

**OPTIMIZED DESIGN OF
PHOTONIC CRYSTAL-BASED INFRARED OBSCURANTS**

by

William West Maslin, III

A thesis submitted to the Faculty of the University of Delaware in partial fulfillment of the requirements for the degree of Master of Science in Electrical and Computer Engineering

Spring 2014

© 2014 William West Maslin, III
All Rights Reserved

UMI Number: 1562401

All rights reserved

INFORMATION TO ALL USERS

The quality of this reproduction is dependent upon the quality of the copy submitted.

In the unlikely event that the author did not send a complete manuscript and there are missing pages, these will be noted. Also, if material had to be removed, a note will indicate the deletion.



UMI 1562401

Published by ProQuest LLC (2014). Copyright in the Dissertation held by the Author.

Microform Edition © ProQuest LLC.

All rights reserved. This work is protected against unauthorized copying under Title 17, United States Code



ProQuest LLC.
789 East Eisenhower Parkway
P.O. Box 1346
Ann Arbor, MI 48106 - 1346

**OPTIMIZED DESIGN OF
PHOTONIC CRYSTAL-BASED INFRARED OBSCURANTS**

by

William West Maslin, III

Approved: _____

Mark S. Mirotznik, Ph.D.
Professor in charge of thesis on behalf of the Advisory Committee

Approved: _____

Kenneth E. Barner, Ph.D.
Chairperson of the Department of Electrical and Computer Engineering

Approved: _____

Babatunde A. Ogunnaike, Ph.D.
Dean of the College of Engineering

Approved: _____

James G. Richards, Ph.D.
Vice Provost for Graduate and Professional Education

ACKNOWLEDGEMENTS

Mark Mirotznik, Ph.D. for his continuous advice, guidance, and academic support during the past several years, as well as his patience for my perfectionistic tendencies.

My professional friends and colleagues, who have supported and helped me throughout my graduate education. Special mention goes to Mr. James Murray as a coworker and invaluable friend.

This manuscript is dedicated to:

My mother, for her endless guidance and unconditional love over the years

My father, for his inspiring intellect and selflessness,
and who I know still watches over me from above

My sister, for the shining example she has set for me

TABLE OF CONTENTS

LIST OF TABLES	vi
LIST OF FIGURES	vii
ABSTRACT.....	ix

Chapter

1 INTRODUCTION.....	1
1.1 Current IR Obscuration Solutions.....	1
1.2 Photonic Crystals: Origins and Significance to Obscuration.....	2
1.2.1 Historical Background.....	2
1.2.2 Application as an Obscurant	3
2 TECHNICAL BACKGROUND	5
2.1 Photonic Crystals.....	5
2.2 Computational Electromagnetic Codes	9
2.2.1 Rigorous Coupled Wave Analysis	10
2.2.2 Finite Difference Time Domain	13
2.3 Optimization Algorithms.....	17
2.3.1 Simulated Annealing.....	17
2.3.2 Pattern Search.....	18
2.4 Obscurant Extinction Coefficient	19
3 DESIGN PROCEDURE – MODELING INFINITE PLANAR SURFACES	21
3.1 Simulation Setup.....	21
3.1.1 RCWA Setup.....	22
3.1.2 Optimization Setup and Flow	23
3.2 Material Selection.....	28
4 DESIGN PROCEDURE – MODELING SINGLE PARTICLE SCATTERING	30
4.1 Simulation Setup.....	31
4.2 Post-Processing.....	34
5 SIMULATION RESULTS.....	37

5.1	One-dimensional Photonic Crystal Transmittance	37
5.1.1	SWIR Dielectric Mirror	37
5.1.2	SWIR Wavelength Filter.....	39
5.1.3	MWIR Dielectric Mirror	40
5.1.4	MWIR Wavelength Filter	41
5.2	Two-dimensional Photonic Crystal Transmittance	42
5.2.1	2D Layer Stack with Enhanced Polarization Insensitivity.....	42
5.2.2	2D Layer Stack with Enhanced Angular Insensitivity.....	44
5.3	One-dimensional Photonic Crystal Volume Extinction Coefficient	46
6	EXPERIMENTAL VALIDATION	50
6.1	SWIR Dielectric Mirror	50
6.2	SWIR 1D Wavelength Selective Filter.....	52
6.3	MWIR Dielectric Mirror.....	53
6.4	A Note on 2D Wavelength Selective Filters.....	55
7	CONCLUSIONS AND FUTURE WORK	56
	REFERENCES	58
Appendix		
A	CODE SAMPLES	61
A.1	Objective Function of the RCWA-2D Optimization Routine	61
A.2	Objective Function of the 1D Multi-Dielectric Optimization Routine.....	64
A.3	MWIR Auxiliary Lookup Function	67
A.4	Example Grating File for RCWA-2D Solver	68

LIST OF TABLES

Table 1. Comparison of mirror design predicted volume extinction coefficient with measured coefficients of deployed obscurants.....	48
---	----

LIST OF FIGURES

Figure 1. Schematic representation of the three types of photonic crystal periodicity.....	7
Figure 2. Illustrations of (a) 1D PhC with fully reflective PBG, and (b) 1D PhC with defect layer and associated defect mode.	7
Figure 3. A schematic representation of a typical grating geometry seen in the RCW simulations in this work.	11
Figure 4. Diagram showing the concept of diffractive orders in RCWA.	12
Figure 5. The Yee unit cell.	14
Figure 6. Lumerical rendering display of a typical PML boundary.	15
Figure 7. Illustration of wavelength-angle dependence of FDTD broadband sources. ..	16
Figure 8. Illustration of the concept of extinction coefficient, either mass or volume. ...	20
Figure 9. Comparison plots of Figures of Merit for 2 iterative designs in an optimization routine for a window filter.....	25
Figure 10. Flow chart describing the iterative optimization process.	26
Figure 11. MATLAB figure of the simulated annealing optimization routine's various plots.	28
Figure 12. Screenshot of the main windows of the Lumerical GUI.	32
Figure 13. Injection profiles of (a) a broadband source over the whole SWIR band (1.4 μm – 3 μm) and (b) a narrowband source ranging from 2.0 μm to 2.1 μm	34
Figure 14. Schematic design for the dielectric mirror particle.	38
Figure 15. (a) Predicted transmittance at normal incidence, (b) simulation results for the transmittance (dB) of the dielectric mirror stack.....	38

Figure 16. Design for the particle with the transmission window. The thickness of the defect layer is denoted by d_0 .	39
Figure 17. (a) Predicted transmittance at normal incidence, and (b) simulation results for the transmittance (dB) of the dielectric stack with defect layer.	40
Figure 18. (a) Perspective view, and (b) simulated transmittance (dB) over angle and wavelength of the MWIR mirror design.	40
Figure 19. (a) Perspective view, and (b) simulated transmittance (dB) over angle and wavelength of the MWIR filter design.	42
Figure 20. Schematic design for the PhC particle with nanocavities and transmission window.	43
Figure 21. Angular simulation sweeps for (a) the window design without nanocavities, and (b) the window design with nanocavities.	44
Figure 22. (a) Perspective view of the unit cell and (b) Simulation results for the 2D PhC strip defect particle.	45
Figure 23. (a) Model of mirror scatterer particle, and (b) Volume extinction coefficient at normal incidence.	47
Figure 24. Volume extinction coefficient of mirror as a function of angle of incidence.	47
Figure 25. Cross-sectional images of the (a) measured and (b) simulated layer stack for the mirror design.	51
Figure 26. The predicted transmittance of the mirror plotted against what was experimentally characterized by an FTIR.	51
Figure 27. Cross-sectional images of the (a) measured and (b) simulated layer stack for the filter design.	52
Figure 28. The predicted transmittance of the filter plotted against what was experimentally characterized by an FTIR.	53
Figure 29. (a) Perspective view, and (b) simulation / measurement comparison of the MWIR mirror layer stack.	54
Figure 30. Transmittance measurement of the fused quartz substrate used in the experimental samples.	54

ABSTRACT

The design, optimization, and experimental feasibility of a novel solution for infrared obscurants based on all-dielectric photonic crystal particles were examined. Using proven rigorous electromagnetic codes and optimization routines, several photonic crystal designs were conceptualized in the short wave and mid-wave infrared radiation bands and their transmission properties were obtained. A method for determining the signal extinction properties of the particles was also developed. Finally, a portion of the designs were fabricated with industry-standard equipment to validate the process experimentally.

Chapter 1

INTRODUCTION

For as long as humankind has been waging wars, there has been a persistent desire for establishing a battlefield advantage over the opponent for concealment of military activities such as troop and vehicle movements. Smoke screens and related obscuration technology have existed for millennia, typically consisting of some type of slow-burn chemical reaction generating a voluminous plume of opaque smoke to prevent visible detection. As detection technology then evolved to target an entirely different portion of the electromagnetic spectrum, specifically the infrared regime, so too did obscuration technology. Present-day innovations in detection prevention mainly use metallic absorptive particulates alongside established visible obscurants to block infrared radiation.

1.1 Current IR Obscuration Solutions

The canonical morphology for realizing obscurants in the infrared involves metallic particles with high aspect ratios, such as rods and flakes. In the literature, these designs have consistently demonstrated high theoretical volume extinction coefficients from the induced surface plasmon resonance (SPR) on the metal [1-3]. In conjunction with varying

particle geometry, this approach carries an inherent flexibility in being able to tune the SPR to a specific wavelength band.

There are a number of issues which reduce the efficacy of SPR-based obscuration, with the principal difficulty being the innate tradeoff between bandwidth and absorption strength. More geometrically complex designs including a more broadband response also have a less pronounced resonance, so that the task of engineering more complicated frequency responses becomes quite difficult. As an example, the creation of a very narrow window of maximum transmission within a wide rejection band presents a nontrivial engineering challenge to the SPR method.

1.2 Photonic Crystals: Origins and Significance to Obscuration

To address the shortcomings of the SPR approach of obscuration, an entirely different design methodology and family of materials is considered – periodic all-dielectric structures called photonic crystals.

1.2.1 Historical Background

The modern concept of a photonic crystal originally manifested as a relatively simple alternating stack of homogeneous dielectric layers. In 1887, Lord Rayleigh first experimented with the reflection characteristics of a periodic one-dimensional layer stack [4]. He observed that the stack had a spectral band of large reflectivity in one dimension, a characteristic now known as a photonic bandgap.

Another 100 years would pass before the current foundational knowledge of multi-dimensional photonic crystals would be solidified by the seminal work of Yablonovitch [5] and John [6]. Yablonovitch looked at the inhibition of spontaneous emission in solid state laser devices by introducing a spatial modulation of the refractive index in three dimensions in order to affect the electromagnetic density of states of the laser gain material. John investigated this same three-dimensional periodic index idea following Yablonovitch's publication as a way of strongly localizing and controlling photons.

From this theoretical groundwork, the number of journal papers about the design of photonic crystals flourished, ranging in application from low-loss waveguides [7], to high Q resonators [8], selective filters [9], and lenses [10]. While the wavelength domain was initially restricted to microwaves due to the challenges posed in fabrication for nanoscale devices, research undertaken by Thomas Krauss in 1996 unlocked the optical regime through inheriting techniques already present in semiconductor industry [11]. Since then, the nanophotonics community has seen unprecedented progress in modelling and manufacturing photonic crystals within traditional semiconductor material systems, principally silicon and silicon dioxide. Other application areas still remain to be tapped, and the central effort of this work focuses on such a novel application – infrared obscuration.

1.2.2 Application as an Obscurant

Any candidate technology for obscuration over a region of the electromagnetic spectrum should fulfill certain performance and efficacy criteria concerning both the

degree of attenuation of an incoming signal and the invariance of that attenuation in a diversity of conditions and scenarios. Moreover, these criteria should still be satisfied in the interest of developing novel multi-functional obscurants which include narrowband windows for purposes of sensor-detector communication. The proven efficacy of photonic crystals at selectively blocking the propagation of a wide band of frequencies promotes their application for IR obscurants. As will be seen in the forthcoming chapters, the wide reflection band can be further maintained for different incident radiation polarizations and angles by engineering more complex crystal designs.

While reflection and transmission properties of photonic crystals by themselves are a robust mechanism of action for obscuration, these properties should deliver comparable signal attenuation to other obscurant designs already deployed. In order to gauge the attenuation, the PhC is modeled as a discrete particle and placed in a light scattering algorithm. The algorithm returns the particle's extinction cross-section or extinction coefficient after calculating how incident radiation is scattered or absorbed by the particle. This coefficient serves as the traditional performance metric for obscurant attenuation. More information on this metric and how it is obtained can be found in Chapter 2.

Chapter 2

TECHNICAL BACKGROUND

This chapter will discuss the relevant principles and information required to understand the research results presented in later chapters. The first section talks about photonic crystals, their mechanism of operation for obscuration and the physics behind it. The next section describes the two computational electromagnetic codes, Rigorous Coupled Wave Analysis (RCWA) and Finite Difference Time Domain (FDTD), employed for simulations. The third section discusses the core optimization algorithms of the research effort, Simulated Annealing (SA) and Pattern Search (PS). Lastly, an overview of signal extinction in the context of obscurants is given.

2.1 Photonic Crystals

The most succinct definition of a photonic crystal (henceforth abbreviated as PhC) is simply an artificial material with a periodic modulation of the refractive index in 1 or more dimensions, where the period is on the order of the operating wavelength. PhCs have found a number of applications since their discovery over a century ago as waveguides, resonators, filters, and lenses. In particular, the selective filtration functionality is of significance to the research presented in this manuscript.

One distinguishing characteristic of PhCs is the ability to create a band of frequencies which are forbidden for propagation inside the crystal structure – a photonic bandgap, or abbreviated PBG. A similar phenomenon arises in the electronic domain with semiconductor crystal lattices forming electronic bandgaps by virtue of the long range order of the lattice. In contrast to the crystalline material phase dependency for engendering forbidden energy bands for electrons, PhCs depend on a certain geometry and dielectric contrast ($\Delta n > 2$ for a wide PBG) between materials to support a bandgap. By intelligently specifying the geometric dimensions of features in the PhC, as well as the optical properties of the constituent materials, the location and size of the PBG can be tailored to the application at hand. In such a way, a wavelength selective filter can be designed, which comprises part of the current research effort outlined here.

Photonic crystals are typically classified by how many dimensions their periodicity encompasses. A pictorial representation of the 3 types is given in Figure 1. Stacks for a 1D PhC are straightforward to model and fabricate in Figure 1(a). Once 2D and 3D periods are introduced, shown in Figure 1(b) and 1(c) respectively, both the modeling and fabrication become nontrivial. In the consideration of potential designs to explore for this research, the 3D PhCs such as the popular “woodpile” stack [12] were not found to be viable due to the sheer complexity of manufacturing.

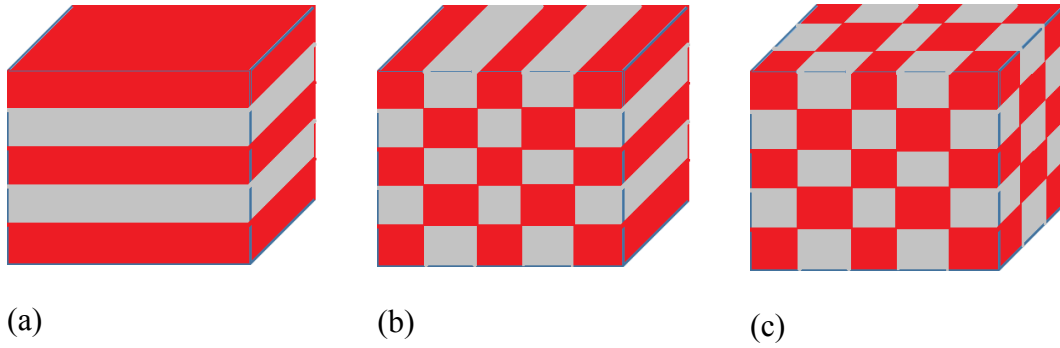


Figure 1. Schematic representation of the three types of photonic crystal periodicity

Depending on how many dimensions constitute the periodic variation, the PhC can exhibit markedly different optical properties. The simplest form is the one-dimensional alternating dielectric stack, seen in the literature under different terminologies. 1D layer stacks as studied by Lord Rayleigh are formed by homogeneous rectangular layers placed alternately on top of each other, so that the refractive index is periodically modulated normal to the stack. An example of this configuration, together with the induced bandgap, is shown in Figure 2(a). Such a structure will be referred to here as a dielectric mirror. Where the dispersion relationship would otherwise hold as the dotted line shown in the plot, a PBG is established that prevents wave propagation, defined in width by those frequencies where standing waves are induced.

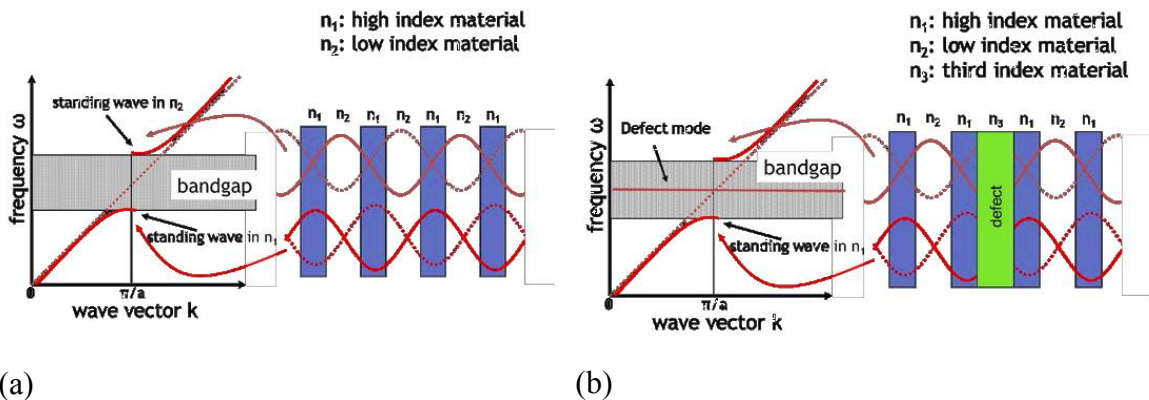


Figure 2. Illustrations of (a) 1D PhC with fully reflective PBG, and (b) 1D PhC with defect layer and associated defect mode.

Two-dimensional approaches to modulating the refractive index involve a checkerboard type arrangement of either a low dielectric filament embedded in a high dielectric matrix (a nanocavity-based design), or a high dielectric filament embedded in a low dielectric matrix (a rod-based design). These complementary approaches demonstrate a duality of both optical properties and polarization sensitivity in the PBG. Rod-based designs exhibit higher rejection of TM modes, while nanocavity-based designs preferentially reject TE modes. Nanocavity-based designs were pursued at the outset of this research due to their superior angular and polarization tolerances over 1D PhCs, and some encouraging modeling results were found, the details of which are in Chapter 5.

Of even greater relevance to the research effort is the formation of propagating modes inside the PBG, termed defect modes. By breaking symmetry of the PhC design using localized point defects or more extended and complicated defects, very narrow transmission windows begin to appear within the forbidden frequencies. This aspect of PhC design is shown in Figure 2(b). While the figure depicts the defect as a third refractive index n_3 interrupting the periodic alteration of n_1 and n_2 , the inclusion of another material isn't strictly necessary to achieve a defect mode.

There is an inherently large degree of design flexibility for inserting a defect into the PhC lattice. The most straightforward method consists of disturbing the periodicity of the layer thicknesses with either a thicker or thinner layer – it avoids the need to incorporate a material with a different dielectric constant than those of the lattice, as Figure 2(b) shows. More unique approaches have been attempted in the literature to much success, such as

altering the doping concentration of the defect layer relative to the surrounding layers [13] and sandwiching two 1D stacks between an anomalous dispersion material [14].

Defects in 2D PhCs constitute an even wider array of options, since they have more degrees of design freedom. Besides breaking symmetry with aperiodic layer thicknesses and refractive indexes to induce defect modes, disruptions in the nanocavity or rod lattice can profoundly change the PBG characteristics. In fact, it has been shown [15] that a common bandgap between TM and TE modes can be optimized by having elliptically shaped air holes interspersed within a hexagonal array of circular holes. Omitting one or more holes in the array can likewise give rise to defect modes supported by a high-Q microcavity [16].

Because the research was focused on minimizing fabrication complexities, the simplest ways of creating a narrow defect passband were emphasized. Chapter 6 will expand upon the choices in particle design in its discussion of the experimental setup.

2.2 Computational Electromagnetic Codes

Several innate characteristics of PhCs provide advantages for computational efficiency in both memory footprint and time. The periodicity of the crystal geometry enables the usage of periodic unit cells that represent a repeated fraction of the overall structure, thus significantly reducing the storage space requirement for the simulation environment. Also, since the PhCs simulated in this work are constructed in well-documented, fairly low loss and dispersionless dielectrics within the SWIR and MWIR

bands, there is no need to formulate an empirically-backed model of optical properties above what is available in material databases.

2.2.1 Rigorous Coupled Wave Analysis

The Rigorous Coupled Wave (RCW) method is a computational electromagnetic method for solving Maxwell's equations for wave diffraction from periodic structures. Over the past 3 decades RCW has served as the foremost analysis technique for computing the electromagnetic response from a variety of grating structures [17-18].

The central idea of RCW is taking advantage of the structural periodicity by expressing the device layers and fields as a Fourier series of spatial harmonics. In particular, the relative permittivity and permeability of each layer become

$$\varepsilon_r(x, y) = \sum_{m=-\infty}^{\infty} \sum_{n=-\infty}^{\infty} a_{m,n} e^{j\left(\frac{2\pi mx}{\Lambda_x} + \frac{2\pi ny}{\Lambda_y}\right)}$$

$$\mu_r(x, y) = \sum_{m=-\infty}^{\infty} \sum_{n=-\infty}^{\infty} b_{m,n} e^{j\left(\frac{2\pi mx}{\Lambda_x} + \frac{2\pi ny}{\Lambda_y}\right)}$$

As a restriction to the dimensionality of the periodic geometry, the setup of a problem in RCW assumes a single dimension for propagation where the device properties per layer are homogeneous, taken as the z -direction in Figure 3. The transverse x and y -directions can then contain an inhomogeneous medium which forms the unit cell of the geometry. The Λ_x and Λ_y are the grating periods in the transverse dimensions. The figure shows a 2D PhC design using 2 materials with different optical properties, and the white circles indicate air-filled nanocavities – the actual inhomogeneity of each individual layer

in the stack. The black shaded box delineates the unit cell that the RCW simulation user specifies, here with the nanocavity fixed at the center of the cell.

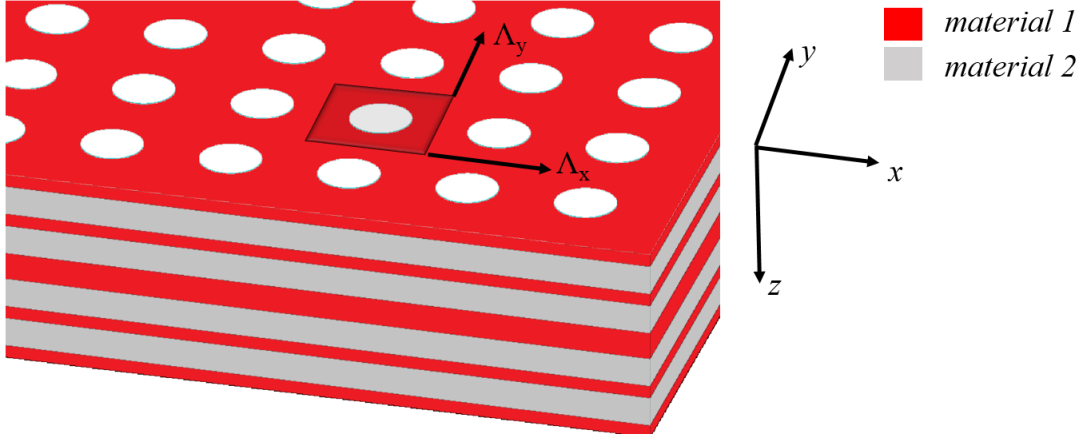


Figure 3. A schematic representation of a typical grating geometry seen in the RCW simulations in this work.

Ensuring accuracy of a RCWA simulation requires that a certain number of diffractive orders be retained in the computation of the solution. Figure 4 shows a visualization of a PhC grating with diffractive orders of the incident field. Here a cross-section of a 2D PhC unit cell is outlined by the dashed lines with nanocavity in the center. In general, the more orders within the computation, the higher the accuracy of the final answers for reflectance and transmittance. Each order has associated with it a diffraction efficiency, a ratio of how much the order is reflected or transmitted compared to the incident wave:

$$DE_{ri} = \operatorname{Re} \left(\frac{\xi_i}{\xi_0} \right) |R_i|^2$$

$$DE_{ti} = \operatorname{Re} \left(\frac{\xi_i}{\xi_0} \right) |T_i|^2$$

where ξ_i / ξ_0 is the ratio of the cosine of the diffraction angle for the i th order wave to the cosine of the diffraction angle of the 0th order incident wave, R_i is the reflection coefficient of the i th order, and T_i is the transmission coefficient of the i th order. The condition for energy conservation follows directly from these efficiencies:

$$\sum_i (DE_{ri} + DE_{ti}) = 1$$

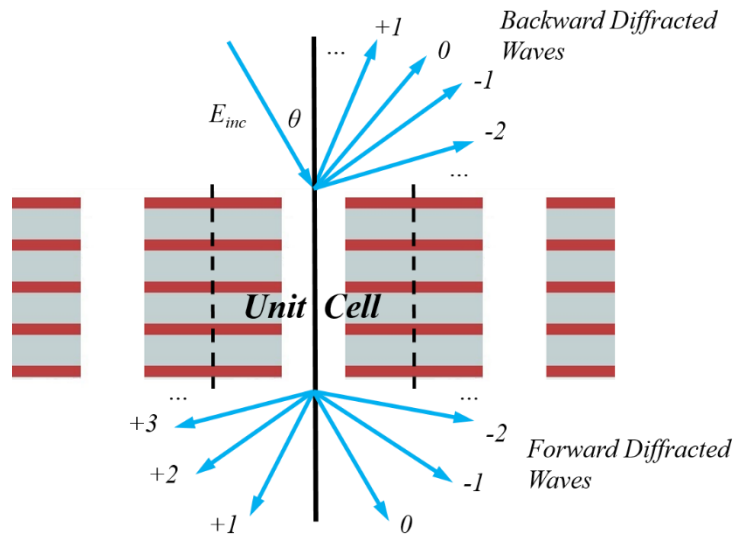


Figure 4. Diagram showing the concept of diffractive orders in RCWA.

RCW carries several advantages over other EM codes within its niche application:

- 1) The method is exact, averting any errors introduced by numerical approximation
- 2) The method is stable, with the only condition on accuracy being the addition of more terms in the spatial harmonic expansion of the field
- 3) The method always satisfies conservation of energy, no matter how many diffractive orders are used

Given these benefits, the RCW technique is immediately applicable to the first stage of PhC obscurant design – modeling the reflectance and transmittance of infinite planar surfaces to discern precise spectral features, e.g., PBG width and defect mode width, of the PhC. Chapter 3 will cover this process in depth.

2.2.2 Finite Difference Time Domain

The Finite Difference Time Domain (FDTD) method is a general-purpose computational electromagnetic algorithm for the solution of the differential form of Maxwell's equations in the time domain. First proposed by Kane Yee in 1966 [19], FDTD consists of the discretization of space in the form of a Yee unit cell (shown in Figure 5) and of the differential equations as central difference equations. In the Yee cell, E field components rest along the edges while H field components lie normal to the center of the cube faces. By staggering the components in this manner, the fields can be solved for at each point in space in a leapfrog fashion according to central differences of the time and space derivatives. The E field vectors update at one instant in time, then the H field vectors update at the next instant in time, and the process is continued until either a minimal energy state is achieved within the simulation volume or a maximum time step is reached.

An FDTD simulation stores a numerical grid of a multitude of Yee cells in computer memory that serve as a discretized analog to a physical structure. To include constitutive material properties of the structure in the grid, electrical permittivity and conductivity values are assigned at E field grid nodes, and magnetic permeability values are assigned at H field grid nodes. This hardwiring material properties into the grid gives

the distinct advantage of easily modeling the electromagnetic response of nonlinear, inhomogeneous, anisotropic, and other exotic media.

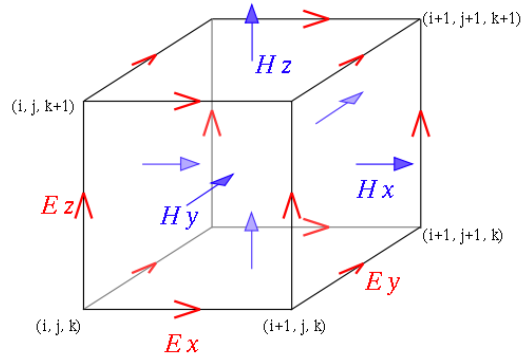


Figure 5. The Yee unit cell.

Image copied under the GFDL license conditions. © Steven G. Johnson, 2005.

Because one of the primary areas of computational modeling for FDTD entails the scattering of incident radiation by free-space obstacles, a method is needed to truncate the simulation space for the finite amount of computer memory available. Initially this truncation was accomplished by cleverly placing PECs on the boundaries where the field was considered outgoing, well beyond the scatterer [19]. However, the most widely used BC implementation today in scattering problems, and the implementation used for the extinction coefficient results in this thesis, is the Perfectly Matched Layer (PML) BC. PMLs were invented by Jean-Pierre Berenger in 1993 [20] to address the constraints on radiation incidence angle of the prevailing BC solution at the time, the Absorbing Boundary Condition. The theory behind PML enables the reflection at the absorbing boundary to be zero for any frequency and any angle of incidence in the computational domain.

A snapshot of a PML boundary as found in the commercial electromagnetic solver, Lumerical© FDTD Solutions, is shown in Figure 6. The orange box is the domain of the FDTD simulation, and its thickness denotes the number of PM layers which is 12 in this case. The number of layers is derived from the user-specified reflection tolerance at the actual boundary, and the finite grid thickness of the PMLs will scale proportionally. A more stringent requirement for stray reflections back into the domain translates to a higher number of PM layers. Also shown is the grid mesh itself, seen in the gray lines interlaced over the screen.

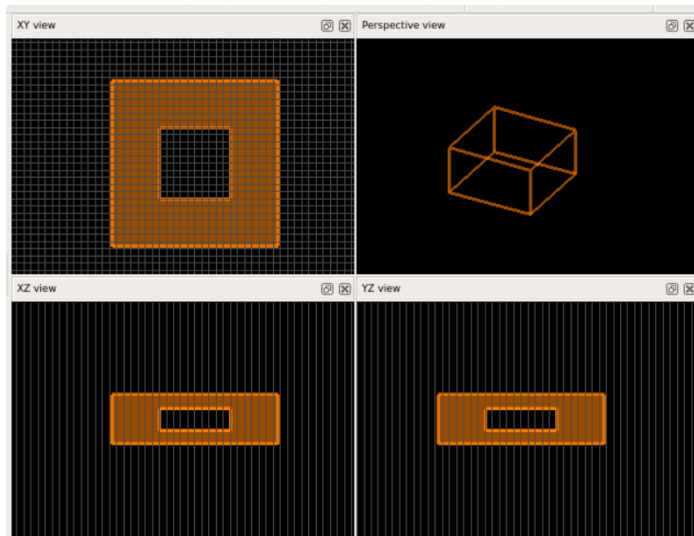


Figure 6. Lumerical rendering display of a typical PML boundary.

Because FDTD seeks to approximate real physical space with a discretized Cartesian grid, several numerical aberrations are introduced which, given a high degree of scrutiny on the part of the user, can be corrected. The most predominant irregularity of FDTD that has affected this research is the concept of grid anisotropy. Essentially, the grid has preferred directions of travel for each wavelength sourced in the computational domain

of the simulation when oblique angles are considered. Figure 7 visualizes this idea in detail. Θ_{inj} is the nominal injection angle of the simulation for operational center wavelength λ_{center} . The in-plane component of the wavevector is constant for all frequencies or wavelengths in the source, and the wavevector itself has a magnitude, the wavenumber, as a function of wavelength:

$$\mathbf{k} = |\mathbf{k}|\hat{\mathbf{k}} = \frac{2\pi}{\lambda}\hat{\mathbf{k}}$$

$$k_{in-plane} = k \sin \theta_{inj}, \quad k_{out-of-plane} = k \cos \theta_{inj}$$

As a consequence, the wavevector out-of-plane component, and by extension, the injection angle, must vary as a function of wavelength. Larger wavelengths are injected at deeper angles, and smaller wavelengths are injected at shallower angles away from the normal. This phenomenon, as will be seen in the procedural documentation in Chapter 4, significantly affected the turnaround time for particle scattering simulations.

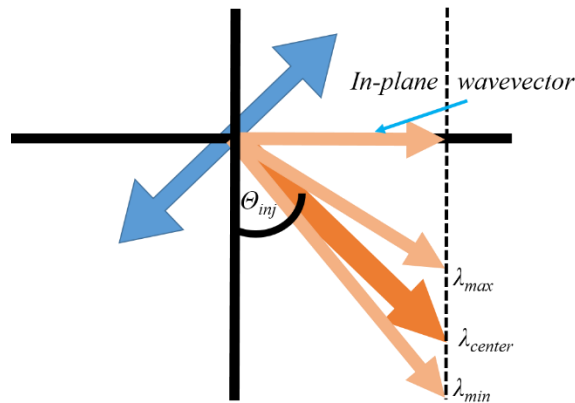


Figure 7. Illustration of wavelength-angle dependence of FDTD broadband sources.

2.3 Optimization Algorithms

The intricate relationships in PhC design between a material's refractive index, layer thickness, and other geometrical parameters exert a profound influence on the location, strength, and angular robustness of the induced PBG. It then becomes a necessary step in design to establish a heuristic for adequately varying these parameters to arrive at a desired solution. In this way, by iteratively navigating the full space of possible parameter combinations – a certain number of periodic layers, particular thicknesses for each layer, as well as hole period and radius in the case of 2D PhCs – one can meet an intended design goal for device performance. Such an iterative approach falls under the moniker of an optimization routine. Here two different types are outlined, each with its respective advantages and disadvantages.

2.3.1 Simulated Annealing

The primary optimization algorithm for PhC design has been simulated annealing (SA). First proposed in 1983 by Kirkpatrick, Gelett and Vecchi [21] and later by Cerny in 1985 [22], SA is a probabilistic method of optimization based on a material science concept known as annealing, a gradual cooling process of a solid material to reduce defects and reach a minimum energy state. The main idea of SA consists of exploring either an unconstrained or constrained solution space to ultimately reach the global minimum of an objective function. The objective function evaluates a vector of input parameters, runs a set of calculations on those parameters, and returns a single scalar “figure of merit” which represents a weight of how the parameters relate to a particular performance metric.

Unique to SA is the notion of temperature, a meta-heuristic governing how far the algorithm searches for a minimum of the objective function. While generally the flow of optimization trends towards a lower FoM, on occasion SA iterates towards points with a higher FoM by virtue of the probability distribution coupled with the temperature. In this way, the algorithm can steer itself out of a space of local minima and search for a global minimum. Eventually, with the influence of the annealing schedule to gradually decrease the temperature, SA converges to a globally optimal result.

As a problem with real-world applications, obscurant design necessitates the constraining of the space on the grounds that optimal designs be physically realizable. Both upper and lower limits are specified in SA for all the PhC variables of interest – refractive index, layer thickness, number of layers, hole period, and hole radius.

2.3.2 Pattern Search

After an attractive design candidate is reached at the conclusion of a SA routine, additional fine-tuned adjustments to the characteristics should be facilitated with an algorithm that quickly makes comparatively minor changes to the design features. Pattern Search (PS) was selected for precisely this process. The idea and coinage of the term PS were proposed by Hooke and Jeeves in 1961 [23] and since then it has gained traction as an optimization routine from its simple approach towards navigating a solution space.

Alternately known as a “Direct Search” method, PS works by varying a single parameter of the initial problem at a time – for PhCs, this variation corresponds to incrementing or decrementing a layer thickness or nanocavity period by a fixed step size –

and re-evaluating the new geometry. Like SA, PS rates a design with a figure of merit, and so when an iterative geometry scores worse than a previous design due to the step size, that size is halved and the process repeats itself. In this way, the optimal solutions that PS produces are local minima rather than truly global minima, which is ideal for expedited calculation of refined designs where only a slight change in performance is desired. In contrast, re-running SA for a slight change would result in the entire solution space being re-explored, significantly extending the computation time.

2.4 Obscurant Extinction Coefficient

Particulate obscurants, whether in the visible, infrared, or another part of the electromagnetic spectrum, use the volume extinction coefficient γ (in units of m^2/cm^3) or mass extinction coefficient α (in units of m^2/g) related by the particle density, in order to quantify how efficiently a candidate obscurant design can attenuate a signal through a particle cloud. Obtaining this metric via computational modeling then becomes an integral step in obscurant design and performance characterization. This section will give a brief exposition into what this metric signifies and its relevance to the research effort, and Chapter 4 will expound upon how it is calculated in the context of a FDTD electromagnetic solver.

The extinction or attenuation coefficient of a signal through a scattering center is a function of the irradiance of the incident radiation (its power in Watts per square meter), the total scattered power of the center (in Watts), as well as the concentration density and

path length through the center or cascade of centers. For all of these quantities, the governing equation is the Beer-Lambert law, given here as:

$$I = I_0 e^{-\alpha Cl}$$

where I is the scattered power, I_0 is the incident irradiance, α is the mass extinction coefficient, C is the concentration density (in units of g / m^3), and l is the path length (in units of m). From this equation, the extinction coefficient can be solved for, yielding:

$$\alpha = \frac{-1}{Cl} \ln \left(\frac{I}{I_0} \right)$$

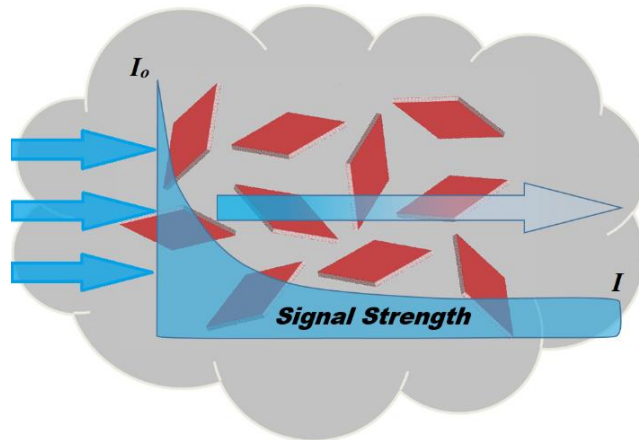


Figure 8. Illustration of the concept of extinction coefficient, either mass or volume.

Figure 8 depicts a graphical representation of the Beer-Lambert Law. As the signal penetrates deeper into the cloud, it loses strength exponentially along the direction of propagation across the physical path length. This loss, the extinction loss, is a combination of scattering and absorptive losses. Ultimately, reports on efficacy in signal attenuation mention the extinction coefficients measured in a testing chamber or range where the Beer-Lambert Law is directly relevant [24-25], but the coefficient can be modeled as well.

Chapter 3

DESIGN PROCEDURE – MODELING INFINITE PLANAR SURFACES

This chapter covers the first of two major steps in the design procedure, which is the computational modeling and optimization of PhC designs to determine transmission and reflection properties in the infrared wavebands. The PhCs are digitally represented as planar surfaces infinite in the dimensions transverse to electromagnetic field propagation.

3.1 Simulation Setup

The main code library utilized for the simulation results which follow in Chapter 5 is the RCWA-2D package available free as a MATLAB toolbox and written by Pavel Kwiecien of the Czech Technical University in Prague, the Czech Republic. Corroborative simulations in 1D were done with another package, the Electromagnetic Waves & Antennas (EWA) toolbox, programmed by Sophocles J. Orfanidis of the ECE Department at Rutgers University.

Objective functions and other code produced or modified by the author can be found in the first section of the Appendix.

3.1.1 RCWA Setup

For standalone use of the RCWA-2D library, as well as use in the context of an optimization algorithm, there are several .m files which must be edited according to the intended application before running a simulation. This section will summarize the alterations that were necessary for each file to accomplish the simulation goals.

main_hexagonal.m or main_rectangular.m

This MATLAB script serves as the front-end interface for the user of the library.

Many important parameters must be specified in this file including:

- 1) Number of diffractive orders to use
- 2) Grating period (relevant for 2D PhCs)
- 3) Superstrate and substrate refractive indexes
- 4) Operating wavelength of the structure
- 5) Incidence angle given as elevation θ and azimuthal ϕ as well as polarization angle, ψ
- 6) Grating file (defines PhC geometry)
- 7) Measurement sweeps, across wavelength, thickness, angle, etc.

hexagonal_grating.m (or other name of the user's choosing)

This script is what is referred to internally as the grating file. It describes the full geometry of the design under test. This enumeration of design parameters includes:

- 1) Number of layers

- 2) Radius of nanocavities in each layer
- 3) Thickness of each layer
- 4) Refractive index of each layer
- 5) Resolution of the grating

After these parameter definitions, the second part of the grating file handles the meshing of the geometry. Given the grating period, resolution, radii, and indexes, the program runs a grid meshing subroutine that outputs three variables. Two are arrays each containing coordinates in x or y which give locations of surface geometry features, ie, changes in refractive index that are encountered as one moves across the surface. The other variable is the matrix of index mesh data.

The final declarations in the file are entries in the `thickness` array, which lists each layer by thickness, as well as assignments of each layer's index profile arranged by the meshing step. Manual changes to this index assignment, such as building larger periodic matrices of differing mesh profiles, allow for the simulation of even more complex 2D designs including secondary defect layer periods. Results which demonstrate this secondary period will be discussed in Chapter 5 under the heading *2D Layer Stack with Enhanced Angular Insensitivity*.

3.1.2 Optimization Setup and Flow

The first step in configuring and launching a simulation optimization routine is the programming of a function which will weigh each iterative PhC design subject to a certain figure of merit. This figure of merit, or FoM, can vary considerably depending on the

application and desired performance metric. Here the FoM was appropriately specified as simply the computation of the total amount of energy allowed through the particle in a given energy band, and then submitted to the algorithm. In the case of the dielectric mirrors, the calculation was done as

$$FoM = \sum_{i = \theta_{min}}^{\theta_{max}} \sum_{j = \lambda_{min}}^{\lambda_{max}} T_{ij}$$

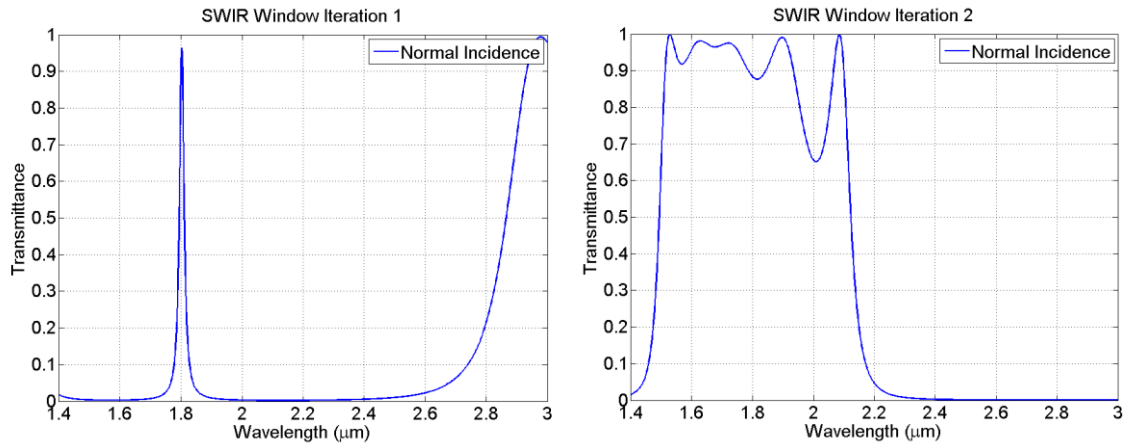
where T_{ij} is the transmittance of the structure at the corresponding wavelength between λ_{min} and λ_{max} and angle of interest between θ_{min} and θ_{max} .

Similarly, for the wavelength selective filters, the most effective FoM would preferentially weigh designs with a maximum transmittance within a particular defect mode band and total reflectance outside that band. As such, the calculation performed was

$$FoM = \sum_{i = \theta_{min}}^{\theta_{max}} \left(\left(\sum_{j = \lambda_{min_out}}^{\lambda_{max_out}} T_{ij} \right) / \left(\sum_{j = \lambda_{min_in}}^{\lambda_{max_in}} T_{ij} \right) \right)$$

In some cases, some augmentations to the FoM formula were added to streamline the arrival at an optimized particle. An example of such an augmentation appears in the objective function written for 1D PhCs, Appendix item A.1.2. Here the reflectance band is divided into two sub-sections, `energy_out_near` and `energy_out_far`, which are energy contributions within and outside a user-specified spectral distance from the narrowband transmittance peak, respectively. The `energy_out_near` total is then exponentiated to carry more influence over the `energy_out_far` total. By splitting the

calculation this way, the algorithm can apply a superior weight to designs in the iteration with very little transmitted energy immediately surrounding the narrowband peak over designs with a wider transmittance plateau at the prescribed wavelength, shown in Figure 9 for a peak wavelength of 1.8 μm .



objective function value of	objective function value of
33.5690	631.2078

Figure 9. Comparison plots of Figures of Merit for 2 iterative designs in an optimization routine for a window filter.

Once the objective function has been programmed, the next step is to select which optimization routine is more appropriate to the current design goal and initialize the inputs to the routine. To initially conceive PhC designs, the SA routine was chosen because it surveys the entire solution space to eventually reach the global minimum of the space. So by defining a desired spectral response metric to score against the objective function FoM, such as a PBG or a defect mode of a particular bandwidth, the SA algorithm will, given enough iteration steps, eventually produce the optimal design for that metric. PS by contrast, surveys a local minimum of the same solution space, and as such, was deemed

more appropriate for design refinement. If the location of the transmission peak or the PBG required shifting, or if the number of device layers had to be adjusted, then PS could be used to a high degree of accuracy for determining the best design suited for a particular goal.

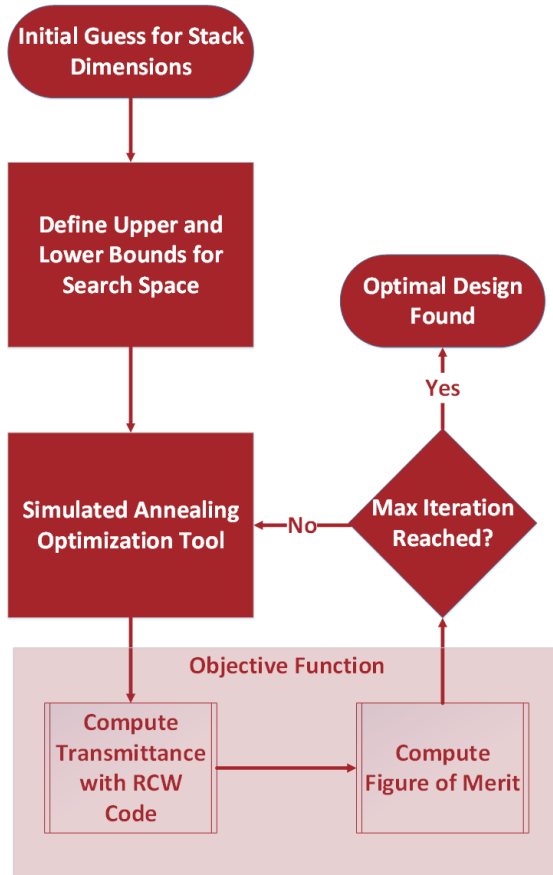


Figure 10. Flow chart describing the iterative optimization process.

as a simulation constraint). The second and third elements are the period and radius in μm respectively. The fourth through sixth elements are refractive indexes of high-n, low-n, and defect layers respectively. The next indexes, elements seven through nine, are high-n, low-n, and defect layer thicknesses in μm . Element ten is the angle of incidence (usually kept constant as another simulation constraint). The eleventh and twelfth elements are related

Figure 10 shows the full design flow chart of the optimization process assuming a run with SA. To begin, a vector of different parameters associated both with the physical design and its spectrum is written as an initial guess for the routine. An example of this vector for a 2D PhC is given below:

$$x_0 = [4 \ 0.7 \ 0.175 \ 3.47 \ 1.45 \ 3.47 \ 0.175 \ 0.4 \ 0.375 \ 0 \ 2.13 \ 0.1 \ 0.5 \ 0.5];$$

Each element index within the vector is labeled as a specific parameter to vary. Here the first element is the number of diffractive orders in the RCWA (usually kept constant

to the FoM – the spectral location of the window (if applicable) and the bandwidth of that window. Finally, elements thirteen and fourteen correspond to advanced design specifications for the 2D geometry, such as a defect layer with a certain ratio of low-index to high-index materials in a strip or fishnet type pattern.

To guarantee manufacturability of the PhCs, boundaries for the search space are declared next. These limitations are of the same format as the initial guess vector with the only difference being the actual value for each aspect of the PhC geometry as either a floor or ceiling dependent on fabrication tolerance. It was found, for instance, that the minimum layer thicknesses that could be reliably fabricated with available Chemical Vapor Deposition (CVD) equipment was 50 nm, and so this value was assigned as the thickness floor of the solution space. Similarly, ceilings on the thicknesses were declared with the knowledge that the total particle thickness could not exceed 5 μm .

The last inputs to the optimization tool concern algorithm-specific options. These options include user interface features like the iterative plotting of the best and current FoM results, maximum number of iterations, command line displays, and other toggle-able preferences. For SA, the following set of statements are made:

```
objectiveFunction = @optimal_rcw2d;
options = saoptimset;
options = saoptimset(options, 'MaxIter' , 5000);
options = saoptimset(options, 'Display' , 'off');
options = saoptimset('PlotFcns', {@saplotbestx,
@saplotbestf, @saplotx, @saplotf});
```

The first statement assigns the objective function handle for the algorithm, @optimal_rcw2d. The remainder of the statements are for configuring SA options,

setting the maximum iterations to 5000, turning off command line feedback, and defining which data points to plot – the best and current values of the geometric and optical parameters and FoM. A MATLAB figure of these plots in a 1D optimization is shown in Figure 11. The convergence of the current best objective function value can be seen.

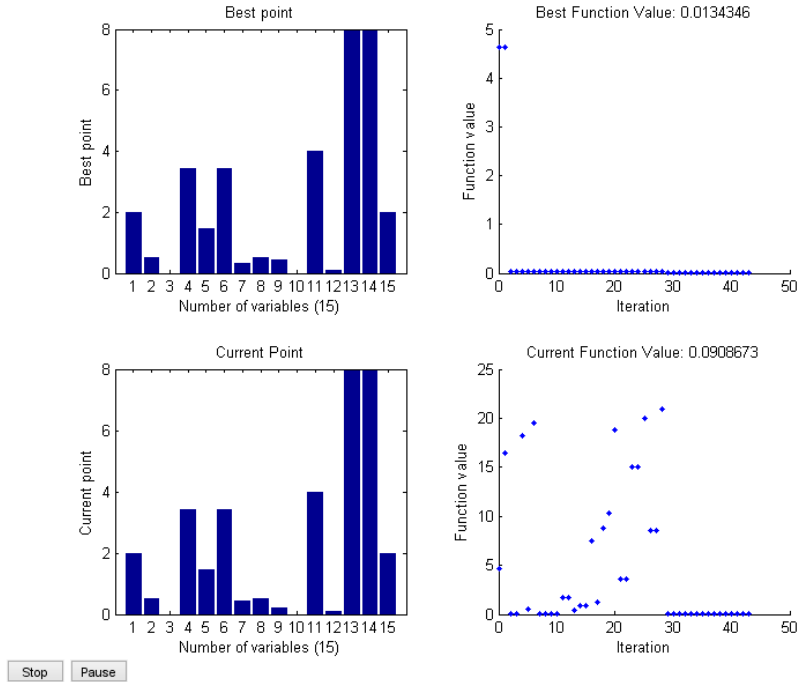


Figure 11. MATLAB figure of the simulated annealing optimization routine's various plots.

3.2 Material Selection

As outlined in the section discussing initial input parameters for optimization, the optical properties of the crystal (specifically, the complex refractive index $n + ik$) were supplied to the algorithm as a general iterative variable with a full breadth of possible values. For the purposes of this research effort, however, certain constant indexes were

selected to model physically realizable compounds with experimentally verified properties in the target infrared bands.

In SWIR, for instance, the high-index material functional in this band was found to be amorphous silicon (a-Si) with a reasonably steady index of $n = 3.47$ across $1.4 \mu\text{m}$ to $3 \mu\text{m}$. Its native oxide, silicon dioxide (SiO_2), possesses an index of $n = 1.45$ in the same wavelength range, conferring the necessary condition of high index contrast ($\Delta n > 2$) for wideband photonic bandgap formation. Both materials were found to have a k -value of 0, termed the extinction loss, in the complex refractive index formulation $\mathbf{n} = n + ik$.

MWIR largely retains the same high index contrast and flat index levels as SWIR with some marked differences. Amorphous silicon continues to have an almost nondispersive refractive index, averaging around 3.43. SiO_2 conversely has a reduction in its index value from 1.42 at the start of the band to 1.34 at the end of the band. Also, beginning at $4 \mu\text{m}$ and continuing to the band edge at $5 \mu\text{m}$, SiO_2 accrues some extinction loss with the value at the edge being $k = 0.00398$, according to the internal material database of Lumerical© FDTD Solutions. A MATLAB function, `mwirLookupSiSiO2`, was written that interpolates the database values into a smooth curve defined at each wavelength. The source code for this function can be viewed in the Appendix A.3.

Chapter 4

DESIGN PROCEDURE – MODELING SINGLE PARTICLE SCATTERING

Obtaining a PhC layer stack with a properly aligned PBG and transmission window is best completed with codes that assume an infinite transverse dimension. Evaluating the PhC's performance as a discrete airborne particulate mandates the use of light scattering codes. To model the particle in the context of a randomized dispersion like a smoke cloud, a single particle scattering paradigm was assumed throughout the process, ie, a scattering event involves only a single particle.

A number of effective and popular scattering codes exist and are being applied to extinction problems, notably the spherical particle scattering approximation method known as Mie theory [26]. However, the planar nature and high degree of inhomogeneity (dielectric constant spatial variation) of the PhC particles pose a modeling challenge to compute an accurate extinction coefficient inside these codes. As mentioned in Chapter 2, one of the main advantages of FDTD is the ability to accurately simulate geometries of arbitrary orientation, shape, size, and electromagnetic inhomogeneity. Furthermore, FDTD is geared towards solving scattering problems, with both the injection of incident plane waves into the simulation space and truncating the space with absorbing boundaries

proving straightforward steps. As such, a commercial FDTD electromagnetic solver package called Lumerical© FDTD Solutions was used to simulate the designs that the optimization routines produced.

4.1 Simulation Setup

A screen capture of the Lumerical Graphical User Interface (GUI) is shown in Figure 12. The perspective and axial views of the geometry under test can be seen, in this case displaying a 1D mirror design. Each of the 9 rectangular layers in the mirror contains parameterized data for the complex index of refraction $n + ik$ imported from a material database internal to the program. The orange box surrounding the rest of the simulation constructs represents the bounds of the FDTD mesh. Since the computation of the scattering cross section is a free space scattering problem, PML boundary conditions were applied to the edge of the mesh.

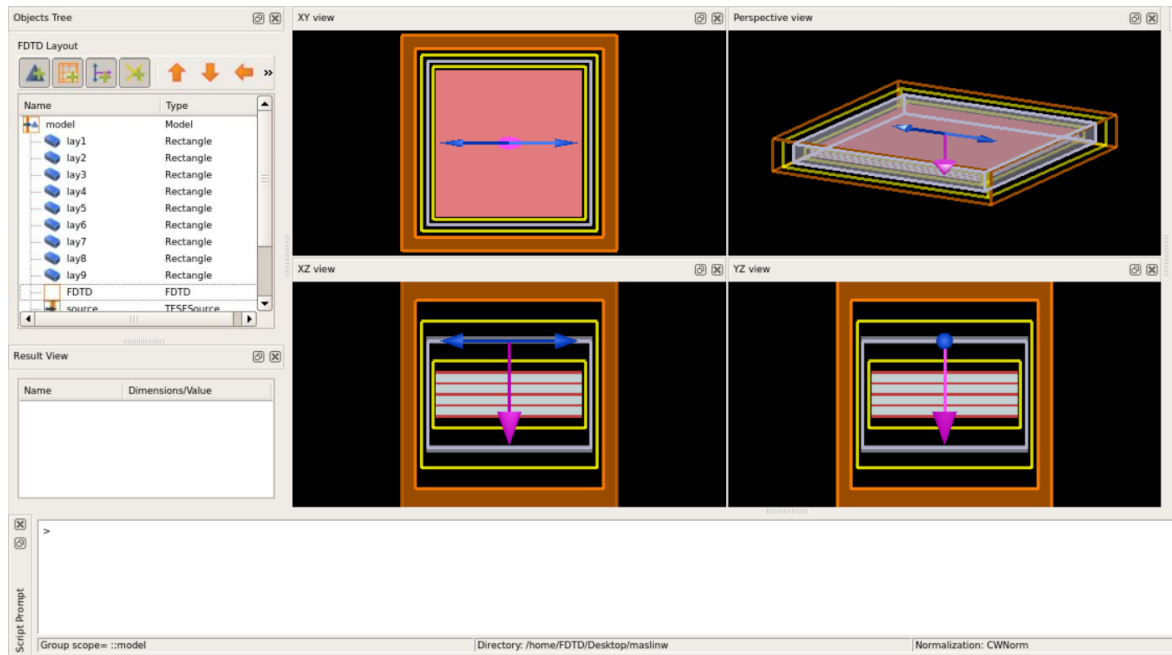


Figure 12. Screenshot of the main windows of the Lumerical GUI.

The gray box with the purple downward directed arrow denotes the source and propagation direction (\mathbf{k} -vector) of the plane wave radiation, the Total Field Scattered Field (TFSF) source. TFSF sources work by segregating the total field into its two constituent components, the incident field and the scattered field. Inside the box, the total field exists with the incident field injected on a particular side of the region (propagation direction given by the purple arrow and polarization given by the blue arrows), and outside the box, only the scattered field is present as the incident field is subtracted at the TFSF region boundaries.

Nested between the edge of the FDTD mesh and the TFSF source, as well as between the source and the design under test, are boxes of power monitors. These monitors collect the transmission data of the FDTD simulation and are referred to by the program as Cross-Section Analysis Groups. The box closest to the particle measures the power

absorbed by the particle, while the outer box enclosing the source measures the power scattered by the particle, since only the scattered field exists in that section of the grid volume.

Expanding the normal incidence setup to oblique angles entails several changes to guarantee accurate results. First, a grid mesh overriding the automatic mesh generation must be included within the entire volume of the TFSF source with a mesh step size equal to the smallest step encountered by the field – in this case, the step for a-Si with its high refractive index. Next, the wavelength range of the source needs to be reduced from a broadband coverage, e.g., the whole SWIR band, to a narrow subset of wavelengths or even a single wavelength. Both of these adjustments are compulsory changes to handle the phenomenon of *grid anisotropy*, introduced in Chapter 2. Since the grid has preferred directions of propagation for any given wavelength, injecting a broadband source would result in an equally wide range of angles actually being tested.

Figure 13 displays the source angular injection profile in a broadband vs. narrowband scenario. The broadband source's angular dependence encompasses a significantly larger field of view than the narrowband source. When the whole SWIR band is covered by the source at a nominal angle of 40° , the actual theta value varies approximately from 30° to 90° . As a consequence, the angular dependence of the particle is vastly distorted by disparate transmission data at different angles. By shrinking the bandwidth of the source, in this case to the wavelength range $2\ \mu\text{m} - 2.1\ \mu\text{m}$, anisotropy is largely averted to within a certain angular tolerance. It was found by the author that a

tolerance of about 1° on either side of the center wavelength ($2.05 \mu\text{m}$ in the figure) was sufficient for accuracy without exorbitantly increasing the computation time.

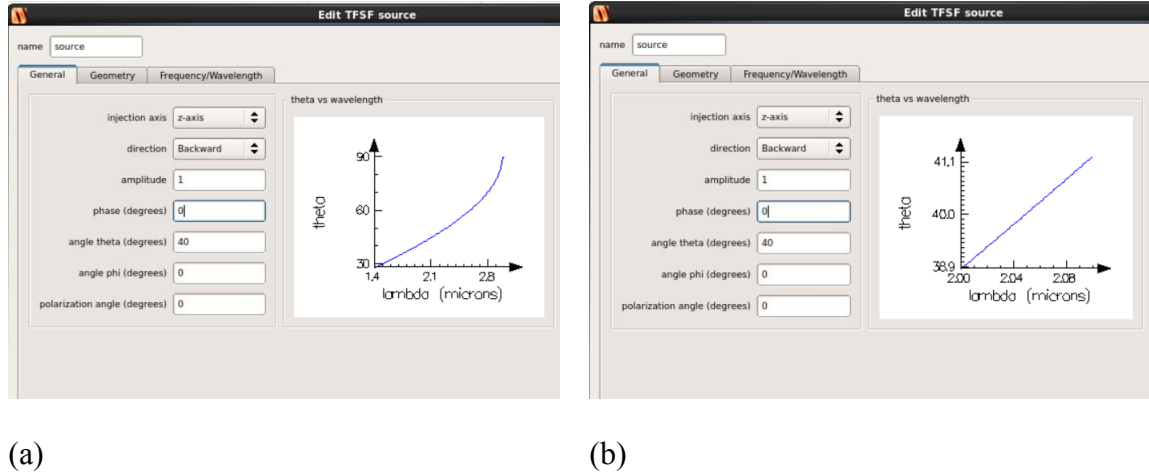


Figure 13. Injection profiles of (a) a broadband source over the whole SWIR band ($1.4 \mu\text{m} - 3 \mu\text{m}$) and (b) a narrowband source ranging from $2.0 \mu\text{m}$ to $2.1 \mu\text{m}$.

4.2 Post-Processing

FTD Solutions contains a rich library of data extraction tools, one of which is the Cross-Section Analysis Tool. It comprises both the Analysis Groups described in Section 4.1 as well as an accompanying script to post-process the field values. The method that the script implements to determine the extinction coefficient differs from that presented in Chapter 2 with Beer's Law. As this problem is treated in a paradigm of single particle scattering rather than multi-particle scattering, there is no concept of a cloud or concentration density, but the extinction metric is nonetheless equivalent insofar as signal strength reduction is concerned.

By isolating the scattered field, one can determine the scattering cross-section σ_{scat} of the design under test with the following relation:

$$P = \sigma_{scat} I$$

where P is the power scattered by the design (in W) and I is the source intensity (in W/m²). Similarly, the absorption cross-section σ_{abs} of the structure can be found by including another encapsulating transmission monitor analysis group directly over the design. This group will return the cross-section as a negative value over the wavelength band of interest to denote power being absorbed across the monitors. The combination of these two cross-sections yields the extinction cross-section, σ_{ext} :

$$\sigma_{ext} = \sigma_{scat} + \sigma_{abs}$$

In the simulations performed in this research, it was found that the σ_{abs} of the PhCs was negligible compared to their σ_{scat} because the materials used, a-Si and SiO₂, have very low loss in the SWIR and MWIR bands. The volume extinction coefficient γ can then be calculated using the extinction cross-section and the particle volume V (in cm³) from the following equation:

$$\gamma = \frac{\sigma_{ext}}{V}$$

Before the data is extracted at the simulation's completion, Lumerical must run a script internal to the Cross-Section Analysis Group that gathers transmission data from all the monitors in the group, sums their power transmission together, and normalizes that total to the source intensity. The output of this script is σ_{scat} or σ_{abs} as a function of wavelength. Also, as another alteration to the raw simulation data in the case of non-normal incidence, the cross-section must be multiplied by the cosine of the tested incidence angle. This step

is done to distinguish how the plane wave source intensity is normalized. By default, Lumerical's `sourceintensity` function computes the intensity normal to the injection plane – either the x , y , or z planes – but at an angle, the extra cosine factor is used to normalize by the intensity normal to the direction of propagation, the \mathbf{k} vector.

Chapter 5

SIMULATION RESULTS

Following the procedures enumerated in Chapters 3 and 4, a number of results were produced in the two infrared bands of interest, SWIR (1.4 μm – 3 μm) and MWIR (3 μm – 5 μm). These results comprised both 1D and 2D PhCs with and without defect-based narrowband transmission windows.

5.1 One-dimensional Photonic Crystal Transmittance

5.1.1 SWIR Dielectric Mirror

Figure 14 shows a perspective and cross-sectional layout of the dielectric mirror design atop a quartz substrate. Values for the legend items were taken as $n_h = 3.47$ (refractive index of a-Si) and $n_l = 1.45$ (refractive index of SiO_2). Relevant layer thicknesses are $d_h = 0.143 \mu\text{m}$ and $d_l = 0.4 \mu\text{m}$ with 9 total layers and a-Si residing on the periphery of the stack, giving a mirror thickness of 2.315 μm .

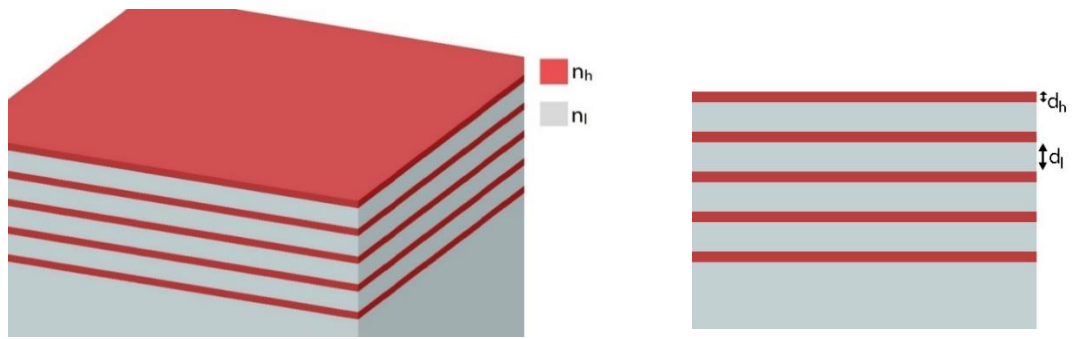
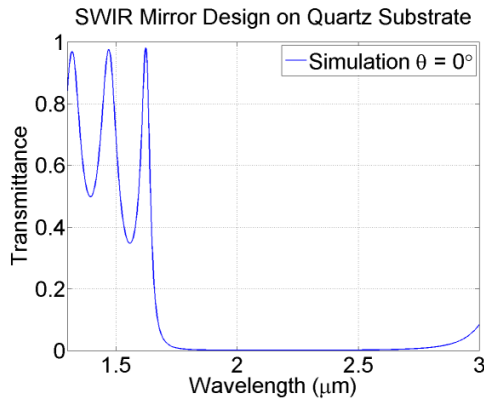
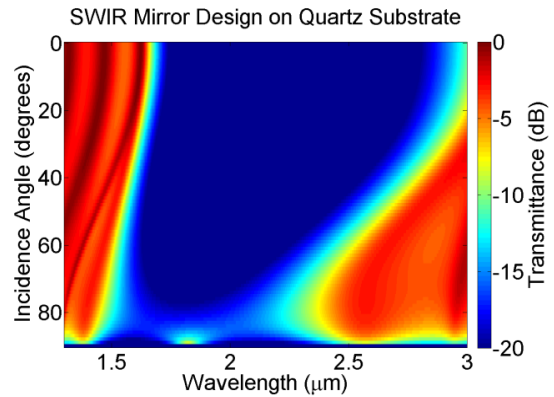


Figure 14. Schematic design for the dielectric mirror particle.

Simulation results for the mirror at normal incidence and across incidence angle are plotted in Figure 15. The data represent an averaged response across TE and TM polarizations. It can be seen that a rejection band of greater than $1.0 \mu\text{m}$ bandwidth and at least -20 dB attenuation is maintained across $0^\circ - 45^\circ$ angles. Beyond 45° , a gradual displacement, shrinkage, and intensity reduction of the PBG occur due to both polarization and angular sensitivities.



(a)



(b)

Figure 15. (a) Predicted transmittance at normal incidence, (b) simulation results for the transmittance (dB) of the dielectric mirror stack.

5.1.2 SWIR Wavelength Filter

The perspective and cross-sectional layout of the wavelength selective filter is given in Figure 16. As with the mirror, the material system consists of a-Si and SiO₂ alternating layers atop a quartz substrate. The stack is 9 layers in total with a defect layer in the center accounting for an aperiodic disturbance in the PhC lattice. Relevant dimensions are $d_h = 0.154 \mu\text{m}$ for the a-Si periodic layers, $d_l = 0.25 \mu\text{m}$ for the SiO₂ layers, and $d_o = 0.33 \mu\text{m}$ for the defect a-Si layer, making the particle $1.946 \mu\text{m}$ in thickness.

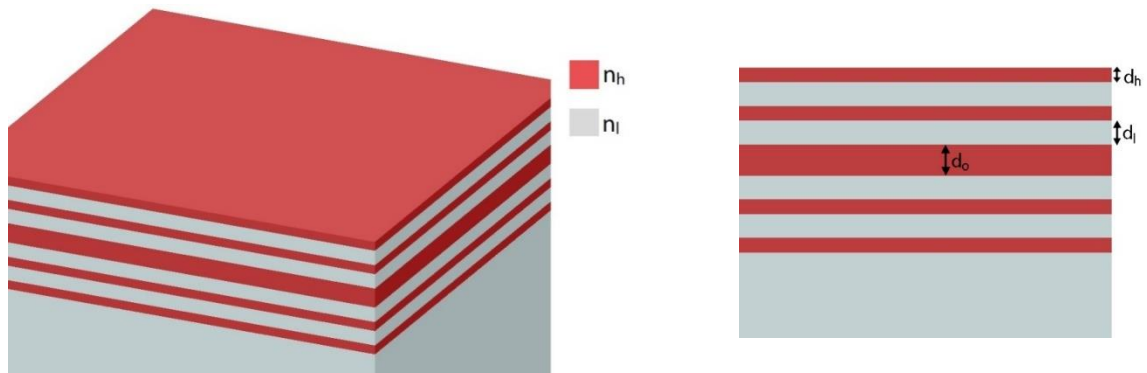
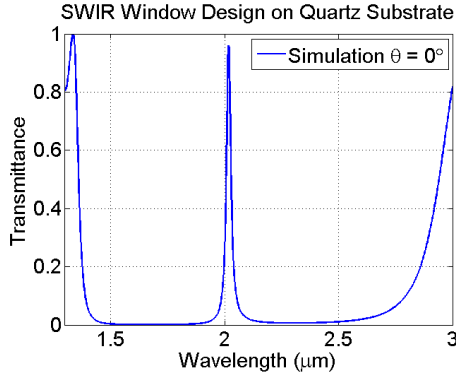
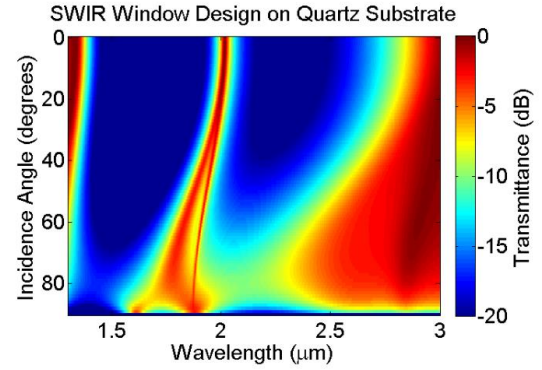


Figure 16. Design for the particle with the transmission window. The thickness of the defect layer is denoted by d_o .

Figure 17 shows the simulation results for the wavelength filter, both at normal incidence and swept across incidence angle. The data represent an averaged response across polarizations. The transmission window engendered by the narrow defect mode in the PBG, centered at $2.017 \mu\text{m}$ inside the stop band with a Full Width Half Max (FWHM) of 22 nm , maintains an amplitude of above 0.95 and negligible spectral shift across the first 30° of angles. It then starts to broaden and migrate over the band at higher oblique angles, eventually leaving a footprint of $0.176 \mu\text{m}$ FWHM at an 80° angle.



(a)

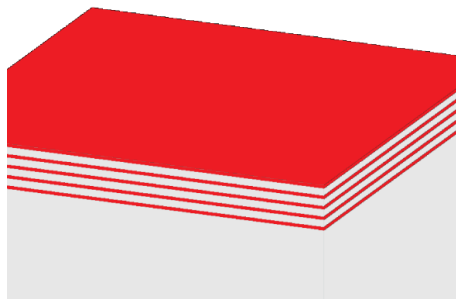


(b)

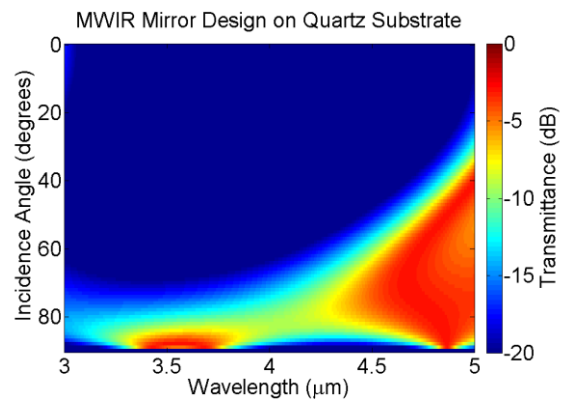
Figure 17. (a) Predicted transmittance at normal incidence, and (b) simulation results for the transmittance (dB) of the dielectric stack with defect layer.

5.1.3 MWIR Dielectric Mirror

Using simple electromagnetic scaling laws to upscale the PhC lattice to longer wavelengths, several designs were produced in the MWIR band with the same material system as that used in SWIR. The first of these designs is a 1D dielectric mirror. The mirror's geometry is shown in Figure 18(a) and strongly resembles the SWIR geometry. Like SWIR, the stack is 9 layers of periodic a-Si and SiO₂ with a-Si layers 0.3 μm thick and SiO₂ layers 0.6 μm thick, yielding a 3.9 μm thick particle.



(a)



(b)

Figure 18. (a) Perspective view, and (b) simulated transmittance (dB) over angle and wavelength of the MWIR mirror design.

The angular sweep of theoretical transmittance for the MWIR mirror is in Figure 18(b). The data represent an averaged response across polarizations. One feature of immediate noteworthiness is the much wider PBG supported by this PhC over the analogous SWIR design. The extra wideness can be attributed to two principal differences. Firstly, the consequences of upscaling the periodicity to accommodate the MWIR regime translate into larger layer thicknesses and a proportionately larger attainable gap. Secondly, the properties of the material system are different between $3\ \mu\text{m} - 5\ \mu\text{m}$ than they are between $1.4\ \mu\text{m} - 3\ \mu\text{m}$. Specifically, the refractive index of SiO_2 decreases over the width of the band from 1.42 to 1.34 while the index of a-Si maintains a fairly steady average value of 3.43. As a result, the index contrast increases across the band from $\Delta n = 2.01$ to $\Delta n = 2.09$, directly influencing the PBG width.

Another change in material properties emerges with the addition of loss in the index of SiO_2 . The extinction coefficient k in $n + ik$ increases from 0 to 0.00398 over MWIR according to the material database within FDTD Solutions. Despite the onset of absorption, the simulated PBG strength is unaffected with a level below -20 dB spanning over $1.5\ \mu\text{m}$ of the band for the first 40° of incidence angles.

5.1.4 MWIR Wavelength Filter

As an upscaled analogy to the SWIR filter, a MWIR filter was simulated as a 1D PhC. The dimensions of the filter, shown in Figure 19(a) above a quartz substrate, are $0.3\ \mu\text{m}$ for the high- n a-Si periodic layers, $0.6\ \mu\text{m}$ for the low- n SiO_2 periodic layers, and $0.55\ \mu\text{m}$ for the defect a-Si layer in the center. It should be noted that this design is simply a

revised version of the mirror design with a thicker center layer to substantiate the principles of defect engineering.

In Figure 19(b), the transmittance of the MWIR filter is swept across angle of incidence. The transmission peak, centered at $3.693 \mu\text{m}$ with a FWHM of 24 nm at normal incidence, undergoes 90 nm of spectral shift in the first 30° of angles with an amplitude of greater than or equal to 0.95 . Again due to angular sensitivity, the peak shrinks to an amplitude of 0.5 and broadens to a FWHM of $0.423 \mu\text{m}$ at an angle of 80° .

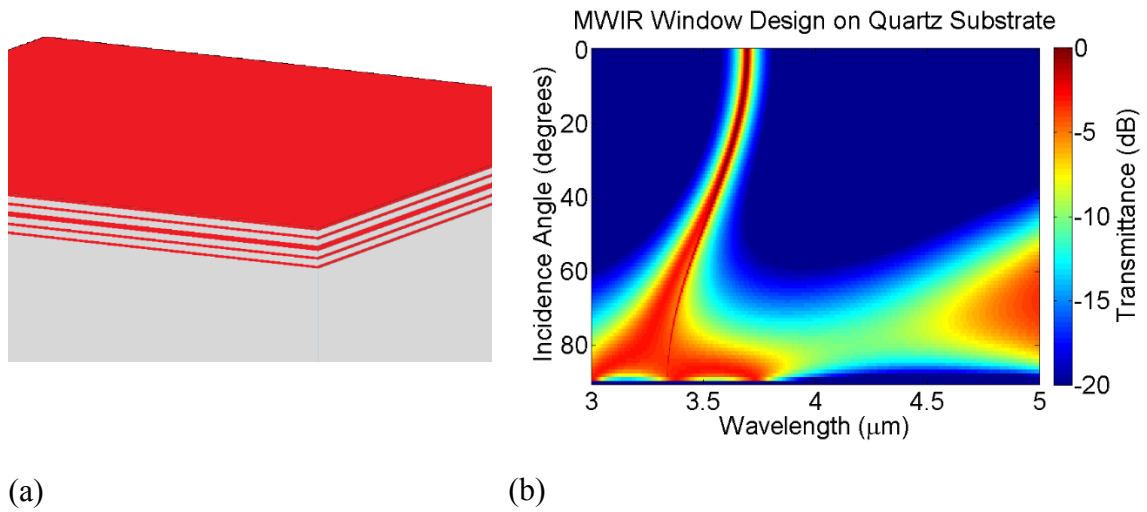


Figure 19. (a) Perspective view, and (b) simulated transmittance (dB) over angle and wavelength of the MWIR filter design.

5.2 Two-dimensional Photonic Crystal Transmittance

5.2.1 2D Layer Stack with Enhanced Polarization Insensitivity

In an effort to improve the angular and polarization sensitivity of the obscurant particles, two-dimensional PhC designs were investigated. Specifically, 2D designs were

simulated with a hexagonally periodic array of circular nanocavities spanning the thickness of the structure. A schematic of this design is given in Figure 20. Relevant dimensions of the stack are $0.175\ \mu\text{m}$ for the high index Si layer, $0.4\ \mu\text{m}$ for the low index SiO_2 layer, and $0.375\ \mu\text{m}$ for the defect Si layer, with a total of 9 layers and thickness of $2.675\ \mu\text{m}$. The holes have a radius of $0.175\ \mu\text{m}$ and are spaced hexagonally with a period of $0.7\ \mu\text{m}$.

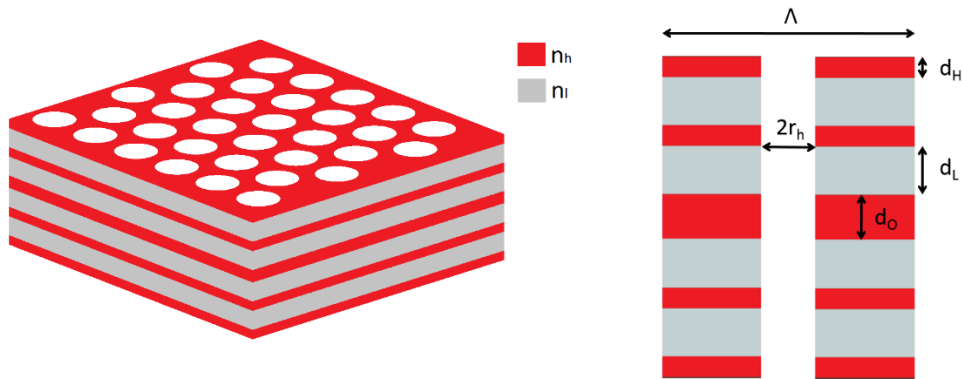


Figure 20. Schematic design for the PhC particle with nanocavities and transmission window.

In Figure 21, the polarization sensitivity of the 1D selective filter is compared against the 2D filter. Across the angles of incidence from 0° to 50° , the 2D filter sustains a more consistent magnitude of the transmission peak for averaged polarizations than the 1D filter. To statistically quantify the improvement, the mean percentage magnitude of the peaks is 84.1% for the 2D with a standard deviation σ of 0.0685 versus a mean of 75.0% for the 1D with a σ of 0.1917 . This result lends credence to the one of the principal benefits of PhC designs of higher dimensionality, namely, the heightened robustness of device performance when tested under different polarizations and angles of the incident radiation.

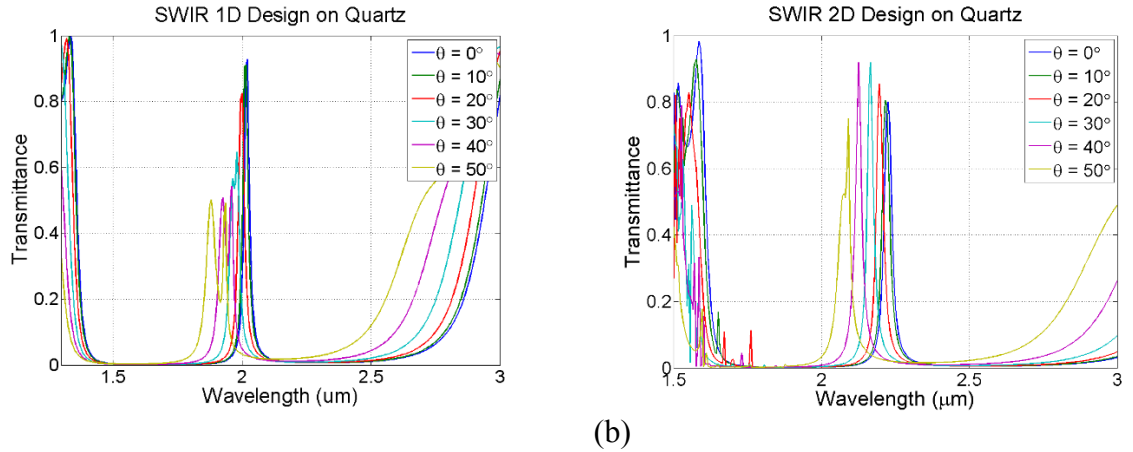


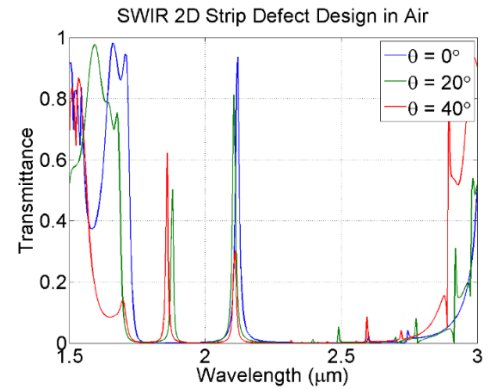
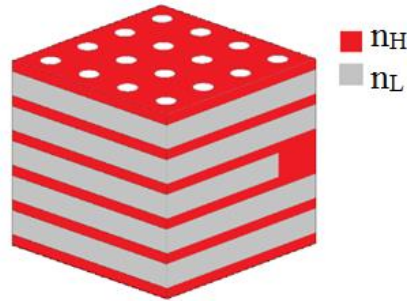
Figure 21. Angular simulation sweeps for (a) the window design without nanocavities, and (b) the window design with nanocavities.

5.2.2 2D Layer Stack with Enhanced Angular Insensitivity

To bolster the angular insensitivity even further when conceiving 2D PhC wavelength selective filters, the manipulation of the defect layer into more complex patterns becomes an integral step in the design process. A landmark paper written by Nakagawa et al. [27] reveals a defect layer design which consists of a secondary strip defect period at an integer multiple ($n \geq 2$) of the nanocavity grating period. Such a defect manifests a ‘wide-field-of-view’ (FoV) resonant cavity inside the PhC, allowing for a spectrally stationary defect mode inside the PBG even at oblique angles of up to 60° . Another paper by Blaike et al. [28] replicated this idea in the millimeter wave regime experimentally with a TM-based 2D PBG and successfully verified the approach.

A rendering of a 9-layer design with $n = 4$ adapted from this wide FoV modality is given in Figure 22(a). In contrast to the layout shown in [27], where the defect strip uses a third refractive index, this stack is constructed from the familiar 2-material SWIR system,

a-Si as the n_H material and SiO_2 as the n_L material. Relevant dimensions of the 11-layer geometry are $0.4828 \mu\text{m}$ for the rectangularly spaced hole grating period, $0.1278 \mu\text{m}$ for the hole radius, $0.245 \mu\text{m}$ for the thickness of the periodic a-Si layers, $0.3347 \mu\text{m}$ for the thickness of the SiO_2 layers, and $0.45 \mu\text{m}$ for the thickness of the defect layer. These values yield a total thickness of $3.2588 \mu\text{m}$ with a secondary defect period of $1.9312 \mu\text{m}$.

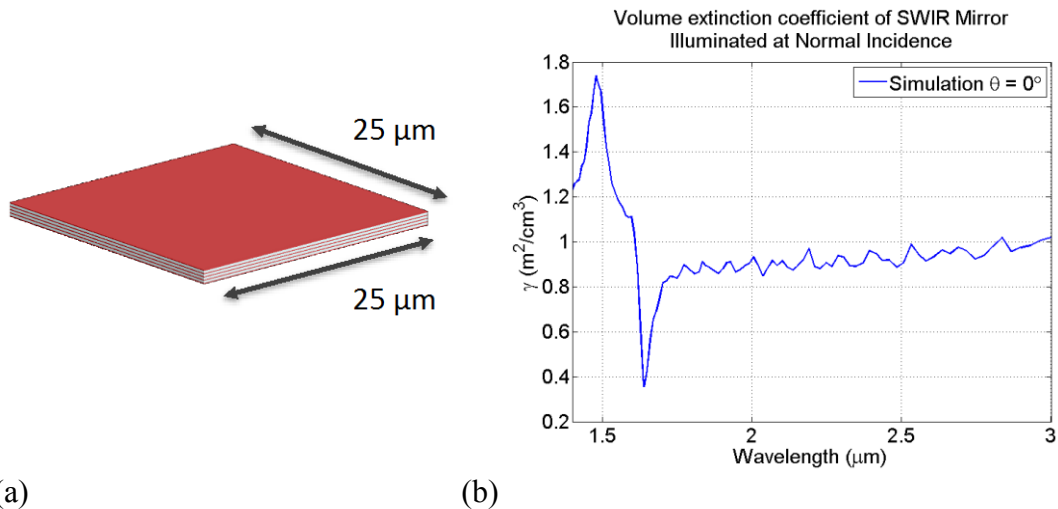


(a) (b)
 Figure 22. (a) Perspective view of the unit cell and (b) Simulation results for the 2D PhC strip defect particle.

The predicted transmittance of the strip design with air cladding is shown in Figure 22(b). The main window peak, centered at $2.12 \mu\text{m}$ with a FWHM of 15.2 nm , shifts only 15 nm in the PBG across the first 40° of incidence angles. Results are for the TE polarization. One observation to be made both within [27] and from this result is that a tradeoff is introduced between the magnitude and position of the peak within the rejection band. At normal incidence, the window has a magnitude of 0.936 , but at 40° , it reduces by over 67% to 0.303 . In a scenario where a stationary passband is desired, such as a communication window through an obscurant particle dispersion, this response is preferable to one where the window leaves a large spectral footprint.

5.3 One-dimensional Photonic Crystal Volume Extinction Coefficient

For PhC obscuration, what determines how effectively a frequency band of interest is rejected is their performance as a particle cloud dispersion. Following the procedure detailed in Chapter 4, the SWIR mirror particle's volume extinction coefficient was calculated across incidence angle and polarization after an extensive battery of FDTD simulations. Figure 23(b) presents the normal incidence result alongside the geometry simulated in Figure 23(a), and Figure 24 presents the band-averaged full angular sweep. The mirror was modeled as a rectangular prism of dimensions $25\ \mu\text{m} \times 25\ \mu\text{m} \times 2.315\ \mu\text{m}$. As might be expected for a 1D PhC where the PBG is supported mainly in the direction normal to the refractive index modulation, the highest γ was achieved at normal incidence with a band-averaged value of $0.9981\ \text{m}^2 / \text{cm}^3$. Due to particle symmetry, as the elevation angle was swept down to $\pm 90^\circ$, the decrease in γ was identical with the lowest value being $0.1891\ \text{m}^2 / \text{cm}^3$ at 90° . It should be noted that the total computational resources and time demanded by this calculation were quite excessive. Interpolations were done between data points for the angular dependence without any loss of accuracy, due to the well-natured, expectable spectral characteristics of this particular PhC.



(a) (b)
 Figure 23. (a) Model of mirror scatterer particle, and (b) Volume extinction coefficient at normal incidence.

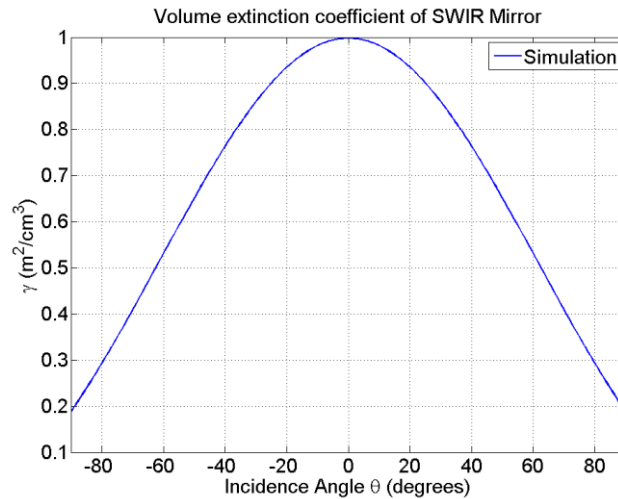


Figure 24. Volume extinction coefficient of mirror as a function of angle of incidence.

Ultimately, gauging where the mirror stands against existing, comparable obscurants is the fundamental task of computational modeling, and the preliminary results show some promise. Table 1 compares the average volume extinction coefficient from the mirror, $0.67 \text{ m}^2 / \text{cm}^3$, with experimentally measured coefficients from a study conducted by Pjesky and Maghirang in 2012 [24]. Only the sodium bicarbonate, ISO fine test dust,

brass flakes, and graphite flakes exceed the theoretical performance of the mirror in their respective infrared bands.

Volume extinction coefficient, m ² /cm ³			
Particle	Mean γ SWIR	Mean γ MWIR	Mean γ LWIR
NanoActive® MgO plus	-	0.33	0.10
NanoActive® MgO	-	0.47	0.07
NanoActive® TiO ₂	-	0.88	0.18
NaHCO ₃	-	1.01	0.89
ISO Fine test dust	-	0.87	0.91
Brass flakes	-	1.50	1.69
Graphite flakes	-	0.75	0.82
Carbon black	-	0.42	0.37
SWIR Mirror*	0.67	-	-

Table 1. Comparison of mirror design predicted volume extinction coefficient with measured coefficients of deployed obscurants.

While the extinction coefficient comparison is promising, several improvements can be applied to the actual particulate geometry. The brass flakes used in the study had a major diameter of approximately 5 μm , the major dimension of their high aspect ratio morphology, and a thickness of less than 500 nm. The PhC mirror tested has considerably larger dimensions, impacting its feasibility in a volume-limited obscurant payload scenario. This size choice was made based on two reasons. First, to preserve the PBG functionality of the PhC, the transverse dimensions of the particle should be large compared to a wavelength – in this case, each side is about 10λ for a SWIR regime particle. Second, it was discovered during fabrication that sonication of the layer stack membrane produced particles with major dimensions in the 20 μm – 30 μm range, so this outcome suitably justifies the trialing of a design with similar feature sizes.

Another limiting factor for obscuration performance of this design is the particulate shape. Since the tested particle is a rectangular prism, it loses the PBG's high-reflectance at steep oblique angles from the direction normal to the stack. Future work is predominantly directed at looking for particles that enhance angular independence from an inherent symmetry. Other geometries yet to be investigated are spherical, cylindrical, and corner reflector-based designs.

Chapter 6

EXPERIMENTAL VALIDATION

As an additional effort above modeling and optimizing PhC obscuration, several of the discussed designs were fabricated and characterized using standard semiconductor industry techniques. The following chapter presents the measured results of fabrication and compares them favorably to the predictions of simulation.

6.1 SWIR Dielectric Mirror

The 1D dielectric mirror layer stack proposed in Section 5.1.1 was deposited using a Plasma-Enhanced Chemical Vapor Deposition (PECVD) system and characterized using a Fourier Transform Interferometer (FTIR). In Figure 24, the model's cross-section is placed adjacent to the real cross-section to highlight the well-controlled deposition parameters. The measured image was obtained from a Scanning Electron Microscope (SEM).

Figure 25 displays the agreement between the simulation predictions and the measurement results for the dielectric mirror. The simulated 97% rejection bandwidth

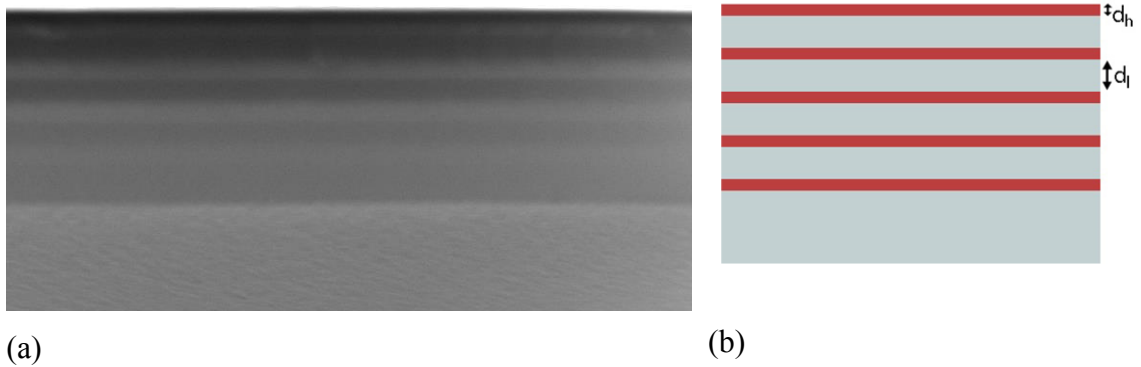


Figure 25. Cross-sectional images of the (a) measured and (b) simulated layer stack for the mirror design.

spans $1.15\ \mu\text{m}$ from $1.7\ \mu\text{m}$ to $2.85\ \mu\text{m}$ while the measured bandwidth spans $1.0\ \mu\text{m}$ from $1.62\ \mu\text{m}$ to $2.62\ \mu\text{m}$. Discrepancies in spectral features, such as the bulge in the experimental plot located between $2.6\ \mu\text{m}$ and $2.8\ \mu\text{m}$ and the overall offset of the graphs, can be explained by differences in material films simulated and fabricated. Specifically, according to the tabulation of fused silica optical properties as listed in [29], an anomalous and sample-dependent absorption band occurs between $2.4\ \mu\text{m}$ and $3.2\ \mu\text{m}$, which is likely responsible for the noisy artifact in that range.

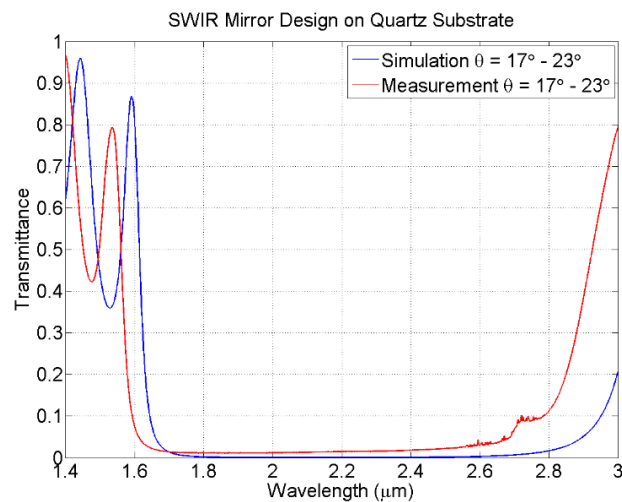


Figure 26. The predicted transmittance of the mirror plotted against what was experimentally characterized by an FTIR.

6.2 SWIR 1D Wavelength Selective Filter

In a similar fashion as the mirror, the SWIR selective filter stack was deposited in the PECVD and had its properties measured by the FTIR. Figure 27 juxtaposes the SEM image and model image for the cross-section, justifying the relative ease of fabrication and precision of the available fabrication equipment.

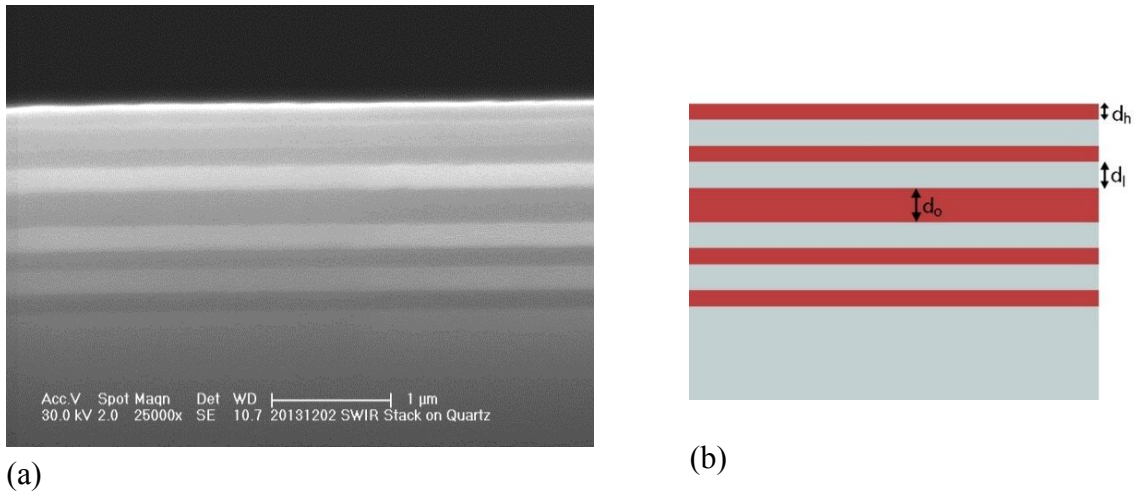


Figure 27. Cross-sectional images of the (a) measured and (b) simulated layer stack for the filter design.

Another experimental validation of the PhC simulations is presented in Figure 28 for the wavelength selective filter discussed in Chapter 5. The simulated 99% rejection bandwidth is 1.17 μm while the measured bandwidth is 1.02 μm. The transmission window peaks of the simulated and measured results are only 17 nm apart, with the simulated resulting in a 79% transmittance peak at 1.998 μm while the measured peak was 66.9% transmittance at 2.015 μm. The FWHM of the simulation and measurements are 29 nm and 39 nm respectively. Further, the filter was characterized 3 separate times to corroborate the results, which agree well in the figure.

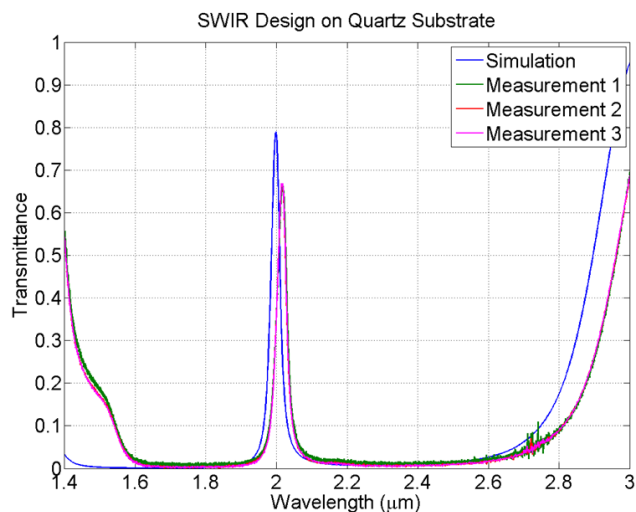


Figure 28. The predicted transmittance of the filter plotted against what was experimentally characterized by an FTIR.

6.3 MWIR Dielectric Mirror

In addition to the 1D particles active in the SWIR band, two MWIR designs were fabricated, characterized, and compared against simulation. In Figure 29, the computed and measured transmittance are given for the MWIR dielectric mirror. The angular range of the transmittance plots correspond to the FTIR optics, 17° to 23° . The size of the 97% rejection bandwidth in simulation spanned the complete MWIR band, while the measured bandwidth is $1.754\ \mu\text{m}$ from $3.016\ \mu\text{m}$ to $4.77\ \mu\text{m}$. The spectral anomaly located between $4.2\ \mu\text{m}$ and $4.37\ \mu\text{m}$ can be attributed to the dispersive effect of the background quartz spectrum measurement, shown in Figure 30. A reduction in transmittance can be seen occurring at the same wavelengths. Likewise, in the last portion of the MWIR band above $4.6\ \mu\text{m}$, an increase in transmittance can be observed in the experimental data versus the predicted data, up to a maximum value of 0.1164 at $4.9965\ \mu\text{m}$. This effect is attributable to the onset

of absorptive losses in the fused silica. According to Figure 30, the transmittance of the quartz drops precipitously to below 10% at about 4.8 μm , which confirms the absorption.

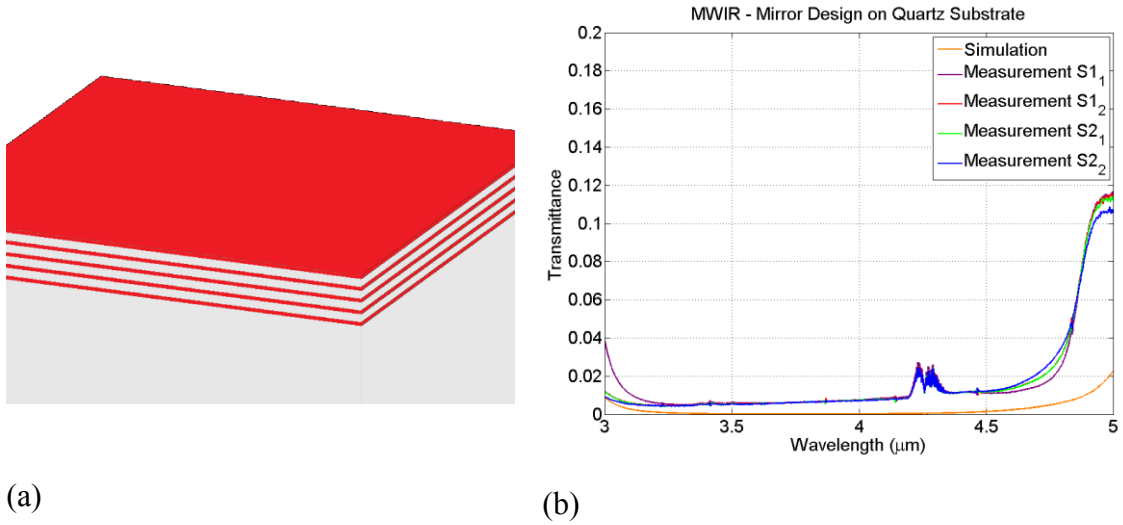


Figure 29. (a) Perspective view, and (b) simulation / measurement comparison of the MWIR mirror layer stack.

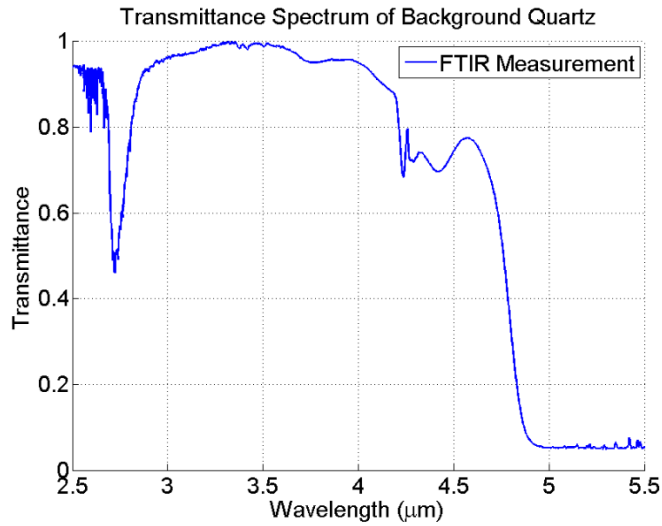


Figure 30. Transmittance measurement of the fused quartz substrate used in the experimental samples.

6.4 A Note on 2D Wavelength Selective Filters

Just as with the 1D PhC designs, the fabrication of the 2D filter was pursued to confirm the modeling computations. Constructing a nanocavity PhC design is a much more difficult engineering challenge, principally because of the high aspect ratio of the nanocavities themselves. In the first design proposed, the aspect ratio of the hole thickness to hole diameter was 7.64 : 1. The second design, the strip defect PhC, had an even greater aspect ratio of 12.75 : 1. The problem at hand for fabrication then became a clever balancing of different etch chemistries between a-Si and SiO₂ to form nanocavities that had straight sidewalls and penetrated the entire depth of the stack without tapering at the bottom. While some encouraging progress was achieved in optimizing the etch, this path towards obscurant manufacture undermines the development of an efficient and highly scalable process for high-throughput deployment of these particles. Alternative avenues are being explored that address the particulate shape and still integrate PBG physics.

Chapter 7

CONCLUSIONS AND FUTURE WORK

A completely new solution to the synthesis of particulate IR obscurants has been proposed and examined which applies the well-known electromagnetic bandgap behavior of photonic crystals as a mechanism of action in obscuration. To address the problems afflicting the SPR-based obscurant particles like brass, especially the inherent limitations in tailoring multi-functional spectral responses with wideband rejection and narrow passbands, the methodology outlined here departs entirely from metallic absorption physics, instead embracing the formation of a forbidden frequency band, or PBG, inside the all-dielectric particle design. Further, a semiconductor industry-standard and potentially highly scalable manufacturing process with extremely cheap and procurable materials upholds the theory behind PhC obscuration with validated measurements.

Given the promising foray into dielectric obscurants, a number of persistent modeling and design challenges were encountered in the course of this research effort. The biggest modeling challenge was the sheer computational size of the scattering problem. FDTD was selected for its broad applicability in particle geometries and affinity for free-space scattering problems and remains a reliable technique to assess extinction properties of the PhC particles. However, due to the high index of a-Si and very large particle size,

the FDTD domain becomes enormous, and measuring extinction at oblique angles substantially increases the simulation time to a point where rapid prototyping of designs is significantly obstructed.

As prospective PhC designs were found, refined in the planar surface simulations, and fabricated to verify theory, the next step in obscurant particle development was the actual design of the aerosolized particulate. To mimic the PhC lattice as closely as possible so as to retain the PBG property, the first design explored was the rectangular prism, 25 μm on a side. This approach had some drawbacks, notably the steep angular dependence of the extinction coefficient and the imprecision with how the prisms were actually manufactured – sonication of the particle membrane yielded very irregular shapes.

Going forward, several alternative geometries with greater angular insensitivity by virtue of their rotational symmetry have been suggested. These geometries fall under the categories of axially, bi-axially, and tri-axially symmetric designs, and they are all candidates to still be investigated in simulation. In particular, spheres with a fused silica core, cylinders, and corner reflectors may prove more effective at extinguishing incident radiation across a broader field-of-view.

REFERENCES

- [1] J. Embury. Maximizing infrared extinction coefficients for metal discs, rods, and spheres. ECBC-TR-226. U.S. Army Edgewood Chemical Biological Center: Aberdeen Proving Ground, MD, 2002.
- [2] P. G. Appleyard and N. Davies. Modelling infrared extinction of high aspect ratio, highly conducting small particles. *Journal of Optics A: Pure and Applied Optics*. 6: 977 – 990, 2004.
- [3] P. G. Appleyard. Modelled infrared extinction and attenuation performance of atmospherically disseminated high aspect ratio metal nanoparticles. *Journal of Optics A: Pure and Applied Optics* 9: 278 – 300, 2007.
- [4] J. W. S. Rayleigh. On the remarkable phenomenon of crystalline reflexion described by Prof. Stokes. *Phil. Mag*, 26: 256 – 265, 1888.
- [5] E. Yablonovitch. Inhibited spontaneous emission in solid-state physics and electronics. *Physical Review Letters* 58(20): 2059 – 2062, 1987.
- [6] S. John. Strong localization of photons in certain disordered dielectric superlattices. *Physical Review Letters* 58(23): 2486 – 2489, 1987.
- [7] L. O’Faolain, X. Yuan, D. McIntyre, S. Thoms, H. Chong, R. M. De La Rue, and T. F. Krauss. Low-loss propagation in photonic crystal waveguides. *Electronics Letters* 42(25): 2006.
- [8] Y. Zhang, C. Zeng, D. Li, G. Gao, Z. Huang, J. Yu, and J. Xia. High-quality-factor photonic crystal ring resonator. *Optics Letters*, 39(5): 1282 – 1285, 2014.
- [9] V. Kumar, A. Kumar, B. Suthar, Kh. S. Singh, and S. P. Ojha. TM polarized filter using 1D photonic crystal. *AIP Conference Proceedings* 1536, 711, 2013.
- [10] T. Decoopman, G. Tayeb, S. Enoch, D. Maystre, and B. Gralak. Photonic crystal lens: From negative refraction and negative index to negative permittivity and permeability. *Physical Review Letters*, 97(7): 073905, 1 – 4, 2006.
- [11] T. F. Krauss, R. M. De La Rue, and S. Brand. Two-dimensional photonic-bandgap structures operating at near-infrared wavelengths. *Nature*. 383(6602): 699 – 702, 1996.

- [12] S. Takahashi, K. Suzuki, M. Okano, M. Imada, T. Nakamori, Y. Ota, K. Ishizaki, and S. Noda. Direct creation of three-dimensional photonic crystals by a top-down approach. *Nature Materials*, 8: 721 – 725, 2009.
- [13] H. C. Hung, C. J. Wu, and S. J. Chang. A mid-infrared tunable filter in a semiconductor-dielectric photonic crystal containing doped semiconductor defect. *Solid State Communications*, 151: 1677 – 1680, 2011.
- [14] L. Jiang-Tao, Z. Yun-Song, W. Fu-He, and G. Ben-Yuan. Ultra-narrow bandwidth optical filters consisting of one-dimensional photonic crystals with anomalous dispersion materials. *Chinese Physics*, 14(12): 2474 – 2477, 2005.
- [15] M. Moghimi, S. Mirzakuchaki, N. Granpayeh, and N. Nozhat. Design and optimization of 2D photonic crystals for the best absolute band gap. *Journal of Theoretical and Applied Physics*, 5-1: 2011.
- [16] O. Painter, J. Vučković, and A. Scherer. Defect modes of a two-dimensional photonic crystal in an optically thin dielectric slab. *Journal of the Optical Society of America B*, 16(2): 275 – 285, 1999.
- [17] M. G. Moharam and T. K. Gaylord. Rigorous coupled-wave analysis of planar-grating diffraction. *Optical Society of America*, 71(7): 811 – 818, 1981.
- [18] M. G. Moharam, E. B. Grann, D. A. Pommet, and T. K. Gaylord. Formulation for stable and efficient implementation of the rigorous coupled-wave analysis of binary gratings. *Journal of the Optical Society of America A*, 12(5): 1068 – 1076, 1995.
- [19] K. Yee. Numerical solution of initial boundary value problems involving Maxwell's equations in isotropic media. *IEEE Transactions on Antennas and Propagation*. 14(3): 302 – 307, 1966.
- [20] J. Berenger. A perfectly matched layer for the absorption of electromagnetic waves. *Journal of Computational Physics*. 114 (2): 185 – 200, 1994.
- [21] S. Kirkpatrick, C. D. Gelett, and M. P. Vecchi. Optimization by simulated annealing. *Science*, 220: 621 – 630, 1983.
- [22] V. Cerny. A thermodynamic approach to the traveling salesman problem: An efficient simulation. *Journal of Optimization Theory and Applications*, 45: 41 – 51, 1985.
- [23] R. Hooke and T.A. Jeeves. "Direct search" solution of numerical and statistical problems. *Journal of the Association for Computing Machinery (ACM)*, 8(2): 212 – 229, 1961.

- [24] S. C. Pjesky and R. G. Maghirang. Infrared extinction properties of nanostructured and conventional particles. *Particulate Science and Technology*, 30: 103 – 118, 2012.
- [25] J. C. Owrutsky, H. H. Nelson, H. D. Ladouceur, and A. P. Baronavski. Obscurants for Infrared Countermeasures II. NRL/FR/6110--00-9945. Naval Research Laboratory: Washington, DC, 2000.
- [26] B. DeLacy, D. Redding, and J. Matthews. Optical, physical, and chemical properties of surface modified titanium dioxide powders. ECBC-TR-835. U.S. Army Edgewood Chemical Biological Center: Aberdeen Proving Ground, MD, 2011.
- [27] W. Nakagawa, P. C. Sun, C. H. Chen, and Y. Fainman. Wide-field-of-view narrow-band spectral filters based on photonic crystal nanocavities. *Optics Letters*, 27: 191 – 193, 2002.
- [28] R. J. Blaikie, T. D. Drysdale, H. M. H. Chong, I. G. Thayne, and D. R. S. Cumming. Wide-field-of-view photonic bandgap filters micromachined from silicon. *Microelectronic Engineering*, 73-74: 357 – 361, 2004.
- [29] W. Rodney and R. Spindler. Index of refraction of fused-quartz glass for ultraviolet, visible, and infrared wavelengths. *Journal of Research of the National Bureau of Standards*, 53(3): 185 – 189, 1954.

Appendix A

CODE SAMPLES

A.1 Objective Function of the RCWA-2D Optimization Routine

```
%optimal_rcw2d.m

function [ FoM ] = optimal_rcw2d( x )
%OPTIMAL_RCW2D This function computes the figure of merit for a 2D
%photonic crystal design as relevant to the obscuration of a particular
%IR band
%{
    Breakdown of the contents of x is as follows:
    x(1): Highest diffractive order (should not exceed 4 for sake of
memory)
    x(2): Period of holes (assuming hexagonal array)
    x(3): Radius of holes
    x(4): Index of high-n layer
    x(5): Index of low-n layer
    x(6): Index of defect layer
    x(7): Thickness of high-n layer
    x(8): Thickness of low-n layer
    x(9): Thickness of defect layer
    x(10): Angle of incidence
    x(11): Center wavelength for transmission window
    x(12): Desired bandwidth of window
    x(13): X-directed fractional percent of high-n material in
checkerboard
    x(14): Y-directed fractional percent of high-n material in
checkerboard
    x(15): Mesh resolution
%}

%xglob is a global variable of optimization inputs to the RCWA-2D
MATLAB
%scripts main_hexagonal and hexagonal_grating
%recglob is a global variable of outputs from the RCWA-2D MATLAB script
%help_control_file
global xglob;
global recglob;
```

```

lambdas = 1.4:0.005:3;
%lambdas = 3:0.005:5;
thetas = 0:10:50;

for q = 1:length(thetas)

x(10) = thetas(q);

%Failsafe loop, in case the period of the nanocavities becomes less
than
%the radius
while (x(2) < 2*x(3))
    x(2) = x(2) + 0.25;
end

xglob = x;

main_hexagonal_SWIR;

%Extracting transmittances from recglob over wavelength
for i = 1:length(recglob)
    rec = recglob(i,:);
    transMat(q,i) = rec(13);
    if (isnan(transMat(q,i)))
        transMat(q,i) = 0;
    end
end

figure(3)
plot(lambdas,transMat(q,:));
drawnow;

end

%Computing the minimum and maximum wavelengths of the window from the
%user-specified center wavelength and bandwidth
[dum lam_min] = min(abs(lambdas-(x(11)-x(12)/2)));
[dum lam_max] = min(abs(lambdas-(x(11)+x(12)/2)));

figure(4)
plot(lambdas,transMat(:, :));
drawnow;

%Running sums of the energy content of the design spectrum, for use in
the
%calculation of the figure of merit
energy_in = 0;
energy_out_near = 0;
energy_out_far = 0;

```

```

%energy inside the passband
for q = 1:length(thetas)
    for i = lam_min:lam_max
        energy_in = energy_in + transMat(q,i);
    end
end
%energy outside the passband
for q = 1:length(thetas)

    %energy closer to the edges of the passband
    %The weights on the actual proximity can vary (here the
energy_out_near
    %is within 3 full passband widths of the real window)
    for i = 4*lam_min-3*lam_max:lam_min-1
        energy_out_near = energy_out_near + transMat(q,i);
    end
    for i = lam_max+1:4*lam_max-3*lam_min
        energy_out_near = energy_out_near + transMat(q,i);
    end

    %energy farther away from the edges of the passband
    for i = 1:4*lam_min-3*lam_max-1
        energy_out_far = energy_out_far + transMat(q,i);
    end
    for i = 4*lam_max-3*lam_min+1:length(lambdas)
        energy_out_far = energy_out_far + transMat(q,i);
    end
end

FoM = (energy_out_far+energy_out_near.^1.25)./(energy_in);
%FoM = energy_in;

fprintf('period of %6.4f, radius of %6.4f, hiN_thick of %6.4f,'...
'loN_thick of %6.4f, def_thick of %6.4f, FoM of %6.4f\n',xglob(2),...
xglob(3),xglob(7),xglob(8),xglob(9),FoM);

end

end

```

A.2 Objective Function of the 1D Multi-Dielectric Optimization Routine

```
%OptiPC_MultiDiel2.m

function FoM = OptiPC_MultiDiel2( x )
%OptiPC_MultiDiel2 This function computes the figure of merit for a 1D
%photonic crystal design as relevant to the obscuration of a particular
%IR band
%{
    Breakdown of the contents of x is as follows:
    x(1): Operating wavelength
    x(2): Index of incident medium
    x(3): Index of transmitting medium
    x(4): Index of high-n material
    x(5): Index of low-n material
    x(6): Thickness of high-n layer
    x(7): Thickness of low-n layer
    x(8): Thickness of defect layer
    x(9): Number of layers on a side (on either side of central layer)
    x(10): Angle of incidence
    x(11): Center wavelength for transmission window
    x(12): Desired bandwidth of window
%}

addpath 'c:\Users\William\Desktop\rcw_code\ewa_code'

%Frequency and wavelength points
c=3e8;
la = linspace(3,5,500);
freq = c./la*1e6;
la0 = x(1);
f0 = c./la0*1e6;

theta = 0:90;

na = x(2);
nb = x(3);
nH = x(4);
nL = x(5);
lH = x(6);
lL = x(7);
lD = x(8);
Nlay = x(9);

%Vector n is the index profile through the layer stack (including
%incident and transmitting media)
n = zeros(length(freq),11);

for i = 1:length(freq)
    %Using the lookup table function for the dispersive index of SiO2
```

```

    [ndisp kdisp] = mwirLookupSiSiO2(c./freq(i)*1e6);
    siO2_Disp = ndisp+li*kdisp;
    %Building the index profile, assuming 9 layers
    n(i,:) = [na nH siO2_Disp nH siO2_Disp nH siO2_Disp nH siO2_Disp nH
nb];
end

%Vector L is the physical length profile of the layer stack
L = [lH,lL,lH,lL,lD,lL,lH,lL,lH];

%Iterating over angle for TE mode transmittance T = 1 - R
for q = 1:length(theta)

T0(q,:) = 1 - abs(multidiel2(n,L/la0,freq./f0,theta(q))).^2;

end

%Iterating over angle for TM mode transmittance T = 1 - R
for q = 1:length(theta)

T0(q+length(theta),:) = 1 - . . .
    abs(multidiel2(n,L/la0,freq./f0,theta(q),'tm')).^2;

end

%%%%%%%%%%%%%%%%%%%%%%%%%%%%%%%%%%%%%%%%%%%%%%%%%%%%%%%%%%%%%%%%%%%%%%%%
%
%
% CODE BLOCK FOR TRANSMISSION WINDOW DESIGN
%
%
%{
energy_in = 0;
energy_out_near = 0;
energy_out_far = 0;
[min_lam min_lam_index] = min(abs(la-(x(11)-x(12)/2)));
[min_lam2 max_lam_index] = min(abs(la-(x(11)+x(12)/2)));

for q = 1:length(theta)
    for i = min_lam_index:max_lam_index
        energy_in = energy_in + T0(q,i);
    end
end

for q = 1:length(theta)
    for i = 4*min_lam_index-3*max_lam_index:min_lam_index-1
        energy_out_near = energy_out_near + T0(q,i);
    end
end

for q = 1:length(theta)
    for i = max_lam_index+1:4*max_lam_index-3*min_lam_index
        energy_out_near = energy_out_near + T0(q,i);
    end
end

```

```

    end
end

for q = 1:length(theta)
    for i = 1:4*min_lam_index-3*max_lam_index-1
        energy_out_far = energy_out_far + T0(q,i);
    end
end
for q = 1:length(theta)
    for i = 4*max_lam_index-3*min_lam_index+1:length(la)
        energy_out_far = energy_out_far + T0(q,i);
    end
end
end
%}
%
%
% END CODE BLOCK
%
%
%%%%%%%%%%%%%%%%%%%%%%%%%%%%%%%%%%%%%%%%%%%%%%%%%%%%%%%%%%%%%%%%%%%%%%%%

%Averaging the TE and TM transmittances
T0tot =
(T0(1:length(theta),:)+T0(length(theta)+1:2*length(theta),:))/2;

%Displaying the data
figure(2)
imagesc(la,theta,10*log10(T0tot),[-20 0])
set(gca,'PlotboxAspectRatio',[8 6 1],'FontSize',22,'XLim',[3 5]);
xlabel('Wavelength (\mum)');
ylabel('Incidence Angle (degrees)');
title('MWIR Mirror Design on Quartz');
c = colorbar;
ylabel(c,'Transmittance (dB)');

figure(5)
plot(la,T0tot(1,:), 'Linewidth',1.5);
drawnow;

%%%%%%%%%%%%%%%%%%%%%%%%%%%%%%%%%%%%%%%%%%%%%%%%%%%%%%%%%%%%%%%%%%%%%%%%
%
%
% CODE BLOCK FOR PURE WIDEBAND MIRROR DESIGN
%
%
%Vector energy is simply the running sum of all the energy allowed
%through the PBG across angles and polarizations
energy = 0;
for q = 1:length(theta)
    for i = 1:length(la)
        energy = energy + abs(T0(q,i));
    end
end

```

```

end
for q = length(theta)+1:2*length(theta)
    for i = 1:length(la)
        energy = energy + abs(T0(q,i));
    end
end
%
%
% END CODE BLOCK
%
%
%%%%%%%%%%%%%%%%%%%%%%%%%%%%%%%%%%%%%%%%%%%%%%%%%%%%%%%%%%%%%%%%%%%%%%%%
%FoM = (energy_out_near.^1.25 + energy_out_far)/(energy_in);
FoM = energy;
fprintf('objective function value of %6.4f\n',FoM);

end

```

A.3 MWIR Auxiliary Lookup Function

```

%Midwave Lookup Function for Wavelength Dependent n = n + ik

function [n k] = mwirLookupSiSiO2(lambda)

lambda_sample = [2.4374 3.2439 3.2668 3.3026 3.422 3.507 3.5564 3.7067
                 3.846 4.167 4.545 5];

n_sample = [1.43095 1.41314 1.41253 1.41155 1.40819 1.40568 1.40418
            1.39936 1.395 1.383 1.365 1.342];

k_sample = [0 0 0 0 0 0 0 0 4.96e-05 0.000107 0.000256 0.00398];

lambda_full = 3:0.001:5;
n_full = interp1(lambda_sample,n_sample,lambda_full);

load xdat.m;
lambmeas = xdat(:,1);
load kmeas.m;
kmeas = kmeas(:,1);

k_full = interp1(lambmeas,kmeas,lambda_full);
[lamval lamind] = min(abs(lambda_full-lambda));

n = n_full(lamind);
k = k_full(lamind);
end

```

A.4 Example Grating File for the RCWA-2D Solver

```
%rectangular_grating.m
%This grating file describes the geometry of the strip defect design
global xglob;
number_of_layers = 11; % this parameter defines number of layers

%Grating period in x and y
Lambda_x = xglob(2);
Lambda_y = Lambda_x; % [um]

%Grating resolution, which defines how finely meshed the cylinders are
resolution_dx=xglob(15);

%radius of the cylinder [um]
r_cylinder = xglob(3);
%thickness of the 1st periodic layer [um]
t_cylinder = xglob(7);
%thickness of the 2nd periodic layer [um]
t_cylinder_2 = xglob(8);
%thickness of the defect layer [um]
t_cylinder_3 = xglob(9);
%refractive index of the cylinder
n_cylinder = 1;
%refractive index of the surrounding layer(s)
n_layer = 3.47;
n_layer_2 = 1.45;
%n_layer_3 = 3.00;

show_grating_mesh=2; % 1=yes, 2=no
%-----
% generation of refractive index mesh
addpath('structures_scripts')
[p_x,p_y,mesh_n_mat]=rectangular_grid(Lambda_x,Lambda_y,resolution_dx,.
..
    r_cylinder,n_cylinder,n_layer,show_grating_mesh);
[p_x2,p_y2,mesh_n_mat2]=rectangular_grid(Lambda_x,Lambda_y,...
    resolution_dx,r_cylinder,n_cylinder,n_layer_2,show_grating_mesh);
%-----

% definition of layer number 1
l=1;

thickness(l)=t_cylinder;

%Vectors indicating where changes/repetitions of surface layer features
%occur. In this case, the unit cell is repeated 4 times in x and y
coordinate_x_1=linspace(0,4*Lambda_x,4*resolution_dx+1);
coordinate_y_1=linspace(0,4*Lambda_y,4*resolution_dx+1);

%matrix of the refractive index grid ;
r_index_1= repmat(mesh_n_mat,4,4);
```

```

%-----
% definition of layer number 2
l=2;

thickness(l)=t_cylinder_2;

coordinate_x_2=linspace(0,4*Lambda_x,4*resolution_dx+1);
coordinate_y_2=linspace(0,4*Lambda_y,4*resolution_dx+1);

r_index_2= repmat(mesh_n_mat2,4,4);

l=3;

thickness(l)=t_cylinder;

coordinate_x_3=linspace(0,4*Lambda_x,4*resolution_dx+1);
coordinate_y_3=linspace(0,4*Lambda_y,4*resolution_dx+1);

r_index_3= repmat(mesh_n_mat,4,4);

l=4;

thickness(l)=t_cylinder_2;

coordinate_x_4=linspace(0,4*Lambda_x,4*resolution_dx+1);
coordinate_y_4=linspace(0,4*Lambda_y,4*resolution_dx+1);

r_index_4= repmat(mesh_n_mat2,4,4);

l=5;

thickness(l)=t_cylinder;

coordinate_x_5=linspace(0,4*Lambda_x,4*resolution_dx+1);
coordinate_y_5=linspace(0,4*Lambda_y,4*resolution_dx+1);

r_index_5= repmat(mesh_n_mat,4,4);

l=6;

thickness(l)=t_cylinder_3;

coordinate_x_6=linspace(0,4*Lambda_x,4*resolution_dx+1);
coordinate_y_6=linspace(0,4*Lambda_y,4*resolution_dx+1);

%This thickness entry is the strip defect layer. The mesh index jumps
%to the high n value from the low n value along the last column of the
%mesh matrix.
r_index_6 = [mesh_n_mat2 mesh_n_mat2 mesh_n_mat2 mesh_n_mat

```

```

mesh_n_mat2 mesh_n_mat2 mesh_n_mat2 mesh_n_mat
mesh_n_mat2 mesh_n_mat2 mesh_n_mat2 mesh_n_mat
mesh_n_mat2 mesh_n_mat2 mesh_n_mat2 mesh_n_mat];

l=7;

thickness(l)=t_cylinder;

coordinate_x_7=linspace(0,4*Lambda_x,4*resolution_dx+1);
coordinate_y_7=linspace(0,4*Lambda_y,4*resolution_dx+1);

r_index_7=repmat(mesh_n_mat,4,4);

l=8;

thickness(l)=t_cylinder_2;

coordinate_x_8=linspace(0,4*Lambda_x,4*resolution_dx+1);
coordinate_y_8=linspace(0,4*Lambda_y,4*resolution_dx+1);

r_index_8=repmat(mesh_n_mat2,4,4);

l=9;

thickness(l)=t_cylinder;

coordinate_x_9=linspace(0,4*Lambda_x,4*resolution_dx+1);
coordinate_y_9=linspace(0,4*Lambda_y,4*resolution_dx+1);

r_index_9=repmat(mesh_n_mat,4,4);

l=10;

thickness(l)=t_cylinder_2;

coordinate_x_10=linspace(0,4*Lambda_x,4*resolution_dx+1);
coordinate_y_10=linspace(0,4*Lambda_y,4*resolution_dx+1);

r_index_10=repmat(mesh_n_mat2,4,4);

l=11;

thickness(l)=t_cylinder;

coordinate_x_11=linspace(0,4*Lambda_x,4*resolution_dx+1);
coordinate_y_11=linspace(0,4*Lambda_y,4*resolution_dx+1);

r_index_11=repmat(mesh_n_mat,4,4);

```